Utilizing Membrane-Anchoring Lipophilic AIEgen for Sonodynamic Therapy against *Toxoplasma Gondii*

Anson Zhang[a]

a. BASIS Bilingual School Shenzhen, No.2 Xinsha Road, Shatou Street, Futian District, Shenzhen, Guangdong, China

Correspondence: anson.zhang90169-bbsz@basischina.com

2026 S.-T. Yau High School Science Award
仅用于2026丘成桐中学科学奖论文公示

ABSTRACT

Aggregation-Induced Emission (AIE) has rapidly developed into a cutting-edge research hotspot spanning chemistry, materials science, biomedicine and optoelectronics. Aggregation-induced emission luminogens (AIEgens) are molecules that exhibit enhanced fluorescence upon aggregation and have emerged as powerful theranostic agents capable of simultaneous fluorescent visualization and cytotoxic reactive oxygen species (ROS) generation for antimicrobial photodynamic therapy (PDT). However, PDT relies on light irradiation, restricting its application to superficial tissues. This limitation presents a major obstacle to completely eradicating deep-seated pathogens such as Toxoplasma gondii (T. gondii), a globally prevalent parasite that establishes lifelong residence within the host central nervous system. Furthermore, the current clinical regimen combining pyrimethamine and sulfadiazine suffers from multiple drawbacks, among which drug resistance is the most prominent. Sonodynamic therapy (SDT), employs low-intensity focused ultrasound (LIFU) instead of light to achieve deep tissue penetration. It functions through dual mechanical (cavitation-induced microjets) and sonochemical (Type I ROS) pathways, representing a promising alternative that remains unexplored for T. gondii treatment. Herein, we developed a membrane-anchoring AIE sonosensitizer (TTP-Mem) for the elimination of T. gondii. TTP-Mem improves SDT efficacy by boosting the production of membrane-proximal ROS to chemically disrupt lipid bilayers. Meanwhile, its Type II ROS production complements the ultrasound-dominated Type I ROS generation, jointly triggering a comprehensive oxidative cascade that initiates lipid peroxidation. In this work, we characterize the synthesis, photophysical properties, membrane affinity, and anti-T. gondii performance of TTP-Mem. Treatment with 5 μM TTP-Mem under SDT (1.5 W/cm^2, 3 min) achieves over 80% reduction in T. gondii viability. This study verifies the feasibility and efficacy of SDT for T. gondii eradication, directly overcoming the drawbacks of slow therapeutic response and drug resistance in current clinical strategies. It provides critical experimental evidence supporting the potential of SDT against deep-seated parasitic infections, offers guidelines for the rational design of sonosensitizers, and delivers valuable insights to tackle relevant public health concerns.

Keywords: Aggregation-Induced Emission (AIE), parasite, *Toxoplasma gondii* (*T. gondii*), Sonoantimicrobial chemotherapy (SACT), Sonodynamic Therapy (SDT), cell membrane, Reactive Oxygen Species (ROS)

2026 S.-T. Yau High School Science Award
仅用于2026丘成桐中学科学奖公示

1. Introduction

Aggregation-Induced Emission (AIE) is a physical phenomenon where certain molecules exhibit greater emission when clustered together, despite them not emitting in free solution. Discovered by Ben Zhong Tang's team in 2001 [1], AIE defies the Aggregation-Caused Quenching (ACQ) phenomenon observed in conventional organic fluorescent dyes like fluorescein where molecules only glow in dilute solutions but dim when concentrated [2], [3]. AIE typically operates via Restriction of Intramolecular Motion (RIM), where the restriction of intramolecular rotation (RIR) or intramolecular vibration (RIV) suppresses non-radiative decay pathways [4], [5]. This initially counterintuitive phenomenon was awarded with the first prize in China's State Natural Science Award and recognized as an IUPAC Top Ten Emerging Technology in 2020. With *Nature* highlighting it to be one of the key nanotechnological materials driving the next nanolight revolution, AIE materials have, since their discovery, transcended disciplinary boundaries [6]. Indeed, they are widely utilized in a variety of areas beyond display technologies and chemical sensing, including biological probes, sensors, anti-counterfeiting, and fingerprint imaging [7], [8], [9], [10]. For example, Sheng et al. reported a NIR-II AIE probe for photoacoustic imaging of orthotopic brain tumors [11]. Importantly, AIE has emerged as a revolutionary tool in pathogen control and the suppression and eradication of infectious disease. Noticeably, AIE molecules used in such applications — specifically antimicrobial photodynamic therapy (PDT) — are usually photosensitizers capable of generating Reactive Oxygen Species (ROS) upon light irradiation, a process conferred by efficient intersystem crossing (ISC) [12], [13]. By narrowing the singlet-triplet energy gap via donor-acceptor molecular engineering, these AIE luminogens (AIEgens) facilitate ISC to generate lethal ROS upon photoactivation [12], [14], [15]. Additionally, in contrast to traditional antibiotics that target specific molecular sites, which makes them vulnerable to resistance mechanisms, ROS eliminates pathogens through oxidative stress to vital microbial components, including DNA, proteins, and lipids [16], [17]. For this reason, AIE-mediated PDT offers a powerful therapy against superbugs. For instance, Li et al. reported using an AIEgens for the simultaneous monitoring and killing of multidrug-resistant bacteria via light-triggered generation of potent ROS [18]. From this perspective, AIEgens are extremely versatile theranostic agents capable of concurrent high-contrast pathogen visualization and potent, light-mediated antimicrobial therapy (reviewed in [14]).

One such example of a drug-resistance pathogen is *Toxoplasma gondii* (*T. gondii*), a zoonotic, protozoan parasite that causes Toxoplasmosis, one of the most pervasive parasitic infections of all endothermic animals, including humans [19]. Indeed, *T. gondii* is widely considered the most successful parasite on earth, estimated to infect nearly one-third of the global population [20], [21], with victims harboring latent infections that persist for months to years, or even indefinitely [22]. Specifically, through initial contact with the parasite via consumption of tissue cysts in undercooked meat or water contaminated with oocysts [19], *T. gondii* rapidly disseminates through blood and lymph from the gut to immunologically-privileged tissues, including the eye, placenta, and the central nervous system (CNS) [23], [24]. Even for immunocompetent hosts, immune response simply controls the infection but does not clear it, ultimately enabling long term infection [22]. Notably, Toxoplasmosis is associated with chronic neurological conditions, such as bipolar disorder [25], schizophrenia [26], [27], [28], [29], seizure from alterations in GABA synthesis [30]; spontaneous abortion or still birth (with primary infection) [21]; and constitutes 30% of all deaths among AIDS patients in Europe [31]. Current clinical strategies primarily rely on clinical drugs that are administered post-infection,

2026 S.-T. Yau High School Science Award
仅用于2026丘成桐中学科学奖公示

most commonly pyrimethamine plus sulfadiazine (P+S) with folinic acid [24], [32], [33]. Although this combination targets both downstream and upstream enzymes in the parasite folate-synthesis pathway (with sulfadiazine targeting DHPS and pyrimethamine targeting DHFR), it has significant limitations: treatment is prolonged, elimination is incomplete (dormant tissue cysts remain), bone marrow is suppressed, and development of resistance is rapid [34], [35]. With the pervasiveness and danger of *T. gondii*, and the limitations of current control strategies, novel AIE-PDT strategies have emerged as a competing alternative, capable of elimination of *T. gondii* through massive generation of ROS, which induces oxidative stress that circumvents drug-resistance on specific pathways. For example, Chen et al. developed a dual Type-I/Type-II AIE photosensitizer that acts through multi-targeted mechanisms to achieve synergistic lethality [36]. However, strategies that rely on light irradiation suffer from a restriction imposed by poor photon tissue penetration, confining its therapeutic efficacy to superficial tissues and leaving deep-seated infections beyond reach [37].

Sonoantimicrobial chemotherapy (SACT), established on the basis of sonodynamic therapy (SDT), offers a solution to the aforementioned limitation. SACT utilizes low intensity focused ultrasound (LIFU) to act on deep-seated pathogens within the tissue, effectively overcoming the depth limitations of conventional PDT [38]. In SDT, a sonosensitizer is used in place of a photosensitizer, and ultrasound is used as the irradiation source instead of photons. Beyond deep penetration, ultrasound provides several advantages via a dual pathway mechanism: (1) a mechanical pathway triggered by the rapid expansion and violent implosion of cavitation-bubbles that generate high velocity microjets that mechanistically disrupt cell membranes [39]; and (2) a sonochemistry oxidative pathway driven by the production of Type I ROS through processes like acoustic pyrolysis [38], [40], [41]. However, SDT's success in treating bacteria (as exemplified in [42]) and biofilms (as shown in [43]) remain completely unexplored in the realm of *T. gondii*, with the additional issue of limited Type II ROS production limiting ultrasound-alone therapy efficacy [44].

Given *T. gondii*'s propensity to form lifelong, deep-seated tissue cysts within the CNS, LIFU is uniquely positioned to address the pathogen; unlike PDT, which is restricted to superficial lesions, ultrasound offers superior tissue penetration alongside spatially adjustable focal precision, enabling non-invasive therapeutic treatment of hard-to-reach sites, ultimately leading to more exhaustive eradication of *T. gondii*. Herein, to the best of our knowledge, we report the first application of SACT for the exhaustive eradication of *T. gondii* using the AIE sonosensitizer TTP-Mem. TTP-Mem is a lipophilic (amphiphilic), positively-charged, polar AIE membrane-anchoring sonosensitizer that exploits a dual-action vulnerability to amplify SDT efficacy: TTP-Mem accentuates the effect of SDT microjets through the generation of membrane-proximal ROS that chemically compromise the bilayer while simultaneously complementing SDT through the generation of Type II ROS. Together, TTP-Mem SDT establishes a comprehensive oxidative cascade that triggers extensive lipid peroxidation. This dual mechanism conferred by TTP-Mem SDT bypasses the drug-resistance issues of traditional P+S regimens while enabling deep-tissue therapeutic penetration of *T. gondii* unachievable by conventional PDT.

In this work, TTP-Mem was synthesized from commercially available material through a two-step reaction featuring a key Knoevenagel-type condensation. Theoretical calculations in Gaussian and experimental characterization of the photophysical properties of TTP-Mem, including its fluorescence and AIE behavior, were performed. The ultrasound-induced TTP-Mem ROS generation efficiency was evaluated via electron

2026 S.-T. Yau High School Science Award
仅用于2026年度科学奖公示

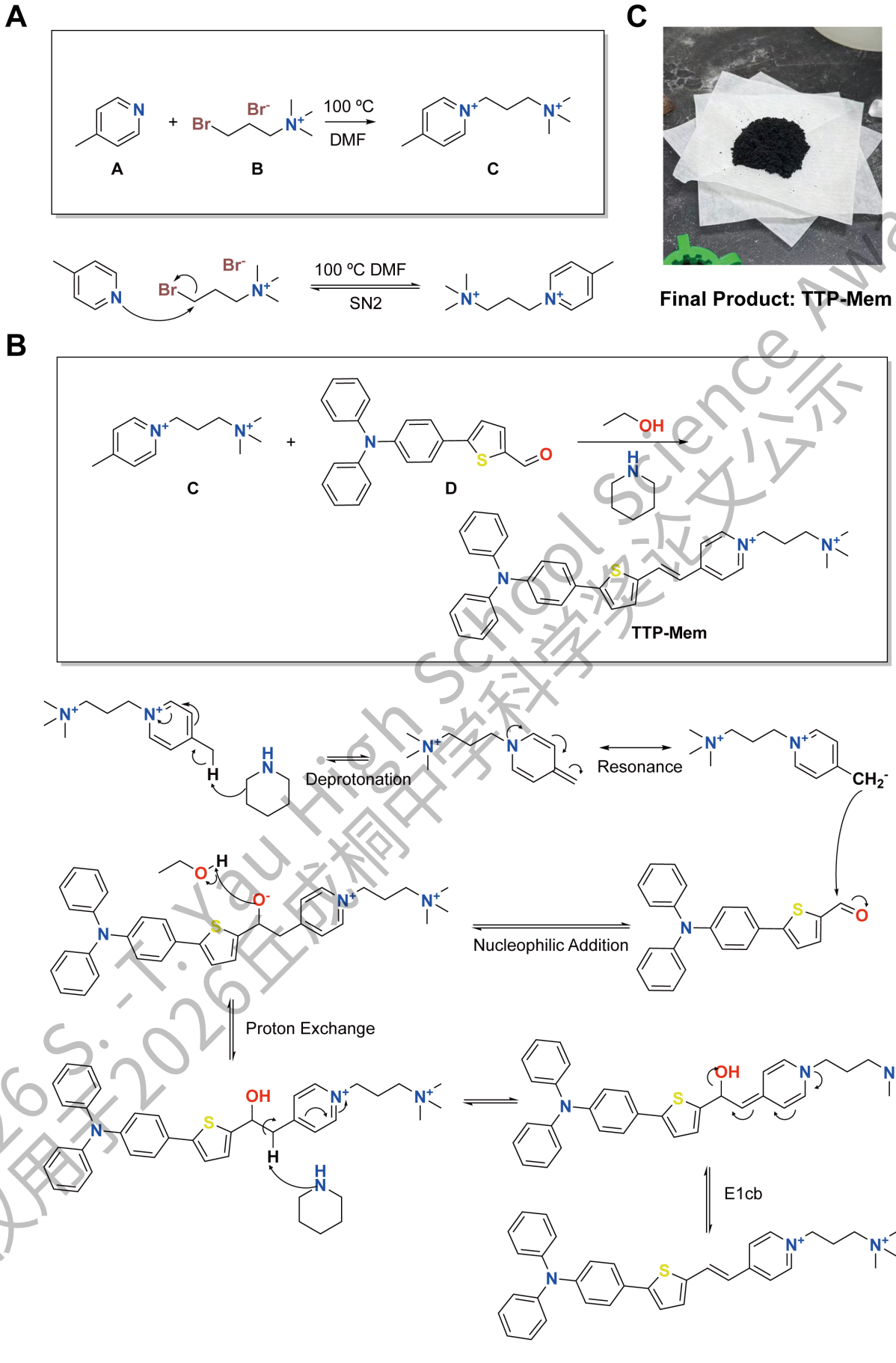
paramagnetic resonance (EPR) spectra and the ABDA absorbance assays. TTP-Mem-membrane anchoring functionalities was simulated via molecular dynamics simulations (MD) and verified experimentally through organelle colocalization analysis. The antiparasitic efficacy of TTP-Mem SDT was evaluated using Calcein/PI (live/dead) staining, with in vitro ROS generation tracked by confocal microscopy using singlet oxygen sensor green (SOSG). Finally, the morphological damage inflicted by TTP-Mem SDT was visualized using scanning electron microscopy (SEM) and crystal violet plaque assays were used to establish TTP-Mem SDT functional therapeutic efficacy in vitro. This study definitively validates the feasibility and efficacy of TTP-Mem SDT in the eradication of *T. gondii* parasites, directly addressing the clinical limitations of existing therapeutic drugs, including slow onset on action and propensity for drug resistance development. Ultimately, the results of this study provide important experimental support for the potential application of sonodynamic therapy in eliminating parasitic infections in deep-seated tissues, offers valuable insights into the rational design and development of AIE sonosensitizer, and holds significant reference value for advancing solutions to public health challenges.

2. Results and Discussion

2.1 Synthesis and Structural Verification of TTP-Mem

The amphipathic, aggregation-induced emission (AIE) molecule TTP-Mem was synthesized through a two step-process (**Scheme 2**). While the synthetic route is adapted from previously reported procedures [45], we propose the following stepwise reaction mechanism based on established organic reaction principles, as no mechanism was previously reported. The first step involves a bimolecular nucleophilic substitution (S_N2) reaction between Compound A (4-methylpyridine) and Compound B (3-bromo-N,N,N-trimethylpropan-1-aminium bromide), where the nucleophilic nitrogen located on the pyridine ring of Compound A attacks the electrophilic alpha carbon of Compound B, substituting the bromine leaving group and forming a quaternary pyridinium salt intermediate, Compound C (4-methyl-1-(3-(trimethylammonio)propyl)pyridin-1-ium) (**Scheme 2A**). The second step involves a complex Knoevenagel-type condensation between the synthesized Compound C and Compound D (5-(4-(diphenylamino)phenyl)thiophene-2-carbaldehyde) (**Scheme 2B**). First, the piperidine solvent deprotonates the hydrogen on the 4-methyl group of Compound C, generating a carbanion stabilized by resonance with the adjacent pyridinium ring. Subsequently, nucleophilic addition occurs as the nucleophilic carbon attacks the alpha carbon on the aldehyde group of Compound D, creating a tetrahedral alkoxide intermediate. Proton exchange with the ethanol solvent then occurs, converting the aforementioned alkoxide into the hydroxyl group. Finally, an E1cB (unimolecular elimination, conjugate base) mechanism then occurs, wherein piperidine deprotonates the hydrogen on the 4-substituted carbon, generating a resonance-stabilized carbanion (again stabilized by the adjacent pyridinium ring). This carbanion's lone electron pair is then used to form a new carbon-carbon π double bond as the hydroxyl leaving group is expelled, yielding the final conjugated TTP-Mem product (**Scheme 2C**). The successful synthesis of TTP-Mem was confirmed via ^{1}H NMR, ^{13}C NMR, and high-resolution mass spectrometry (see **Section 3.1**, **Fig. 14-16**).

2026 S.-T. Yau High School Science Award 仅用于2026丘成桐中学科学奖论文公示



2026 S.-T. Yau High School Science Award
仅用于2026丘成桐中学科学奖论文公示

154

Scheme 2 | Schematic illustration of the reaction mechanism for the synthesis of TTP-Mem. (A) Synthesis of **Compound C** (4-methyl-1-(3-(trimethylammonio)propyl)pyridin-1-ium) via nucleophilic substitution (S_N2) between **Compound A** (4-methylpyridine) and **Compound B** (3-bromo-N,N,N-trimethylpropan-1-aminium bromide). **(B)** Synthesis of TTP-Mem through a Knoevenagel-type condensation between **Compound C** and **Compound D** (5-(4-(diphenylamino)phenyl)thiophene-2-carbaldehyde), annotated with individual mechanistic steps. **(C)** Photograph of the synthesized TTP-Mem in its powdered form, exhibiting a deep magenta/maroon color.

2.2 Photophysical Characterization of TTP-Mem

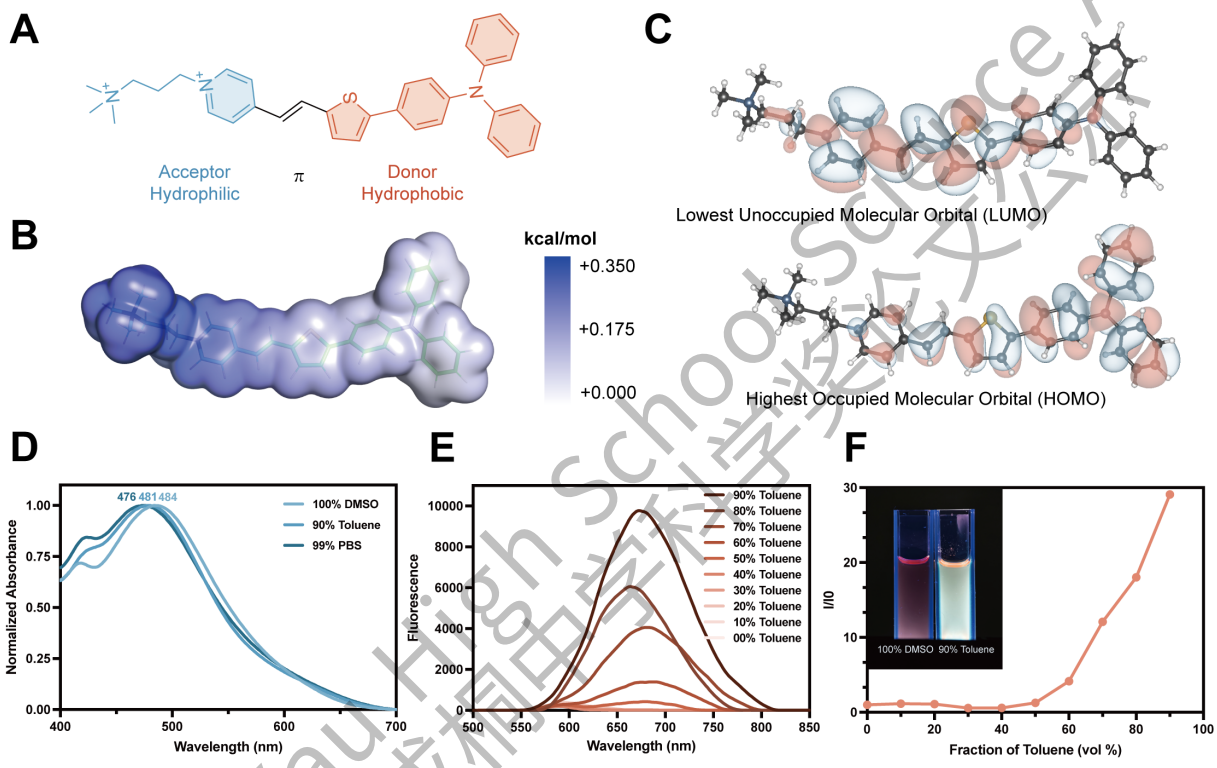


Fig. 1 | Theoretical calculations, photophysical properties, and AIE characteristics of TTP-Mem. (**A-B**) Skeletal scaffold of TTP-Mem with donor-π-acceptor structure (**A**) and electrostatic potential map of TTP-Mem with a cumulation of positive charge in hydrophilic tail (**B**). (**C**) Frontier molecular orbitals (HOMO, LUMO) obtained from Gaussian ground-state DFT calculations. (**D**) Normalized UV-Vis absorption spectra of TTP-Mem under 100% DMSO, 90% toluene/DMSO, and 99% PBS/DMSO. (**E**) Fluorescence emission spectra of TTP-Mem with increasing toluene/DMSO volume ratios (λex = 480 nm). (**F**) Plot of emission maxima (λem) and relative emission intensities (I/I_0, normalized to maximum emission in pure DMSO) versus toluene volume ratio.

The synthesized TTP-Mem molecule was designed with several characteristics (**Fig. 1A-B**). First, it is an amphipathic molecule with a hydrophobic base consisting of three electron-rich triphenylamine group and a hydrophilic tail with high polarity. Electrostatic potential map (ESP) results confirm this proposed design, with cumulation of positive electric potential centered at the hydrophilic tail and near neutral potential centered at the hydrophobic base (Fig. **1B**; see **Section 3.2** for Gaussian calculations). Specifically, the π-electron clouds of the triphenylamine form hydrophobic surfaces is governed by weak induced dipole/van

2026 S-T Yau High School Science Award 仅用于2026日本科学学会大会

der Waals forces, while the two positive charges from the pyridinium nitrogen and the quaternary ammonium salt of the hydrophilic tail engage in strong dipole interactions with the electronegative oxygen atoms on surrounding water molecules. Second, TTP-Mem is an aggregation-induced emission (AIE) molecule. Notably, the triphenylamine–thiophene–pyridinium (TTP) core scaffold was chosen as it features a twisted conjugate framework, allowing for strong donor-π-acceptor (D-π-A) interactions — the triphenylamine serving as an electron-rich donor, thiophene as a π bridge that connects the two conjugated systems, and the pyridinium moiety as an electron receptor with its two positive charges (**Fig. 1A**). This extended D-π-A system promotes Intramolecular Charge Transfer (ICT) and narrows the electronic bandgap, enhancing radiative emission pathways. Furthermore, the twisted propeller-like geometry of the TTP core also hinders cofacial π-stacking between adjacent molecules. Consequently, this suppresses aggregation-induced non-radiative decay pathways, such as exciplex and excimer formation, and instead favors radiative emission (fluorescence) (**Scheme 4**). Overall, these amphipathic and AIE-active design elements were evaluated in silico through density functional theory (DFT), and time-dependent DFT (TD-DFT) calculations, followed by experimental characterization using UV-Vis absorption and fluorescence spectroscopy.

2.2.1 Theoretical Calculations Predict Photophysical Properties of TTP-Mem

To elucidate the photophysical properties of TTP-Mem, Gaussian theoretical calculations were computed and evaluated. Frontier orbitals were extracted from the ground-state geometry optimized TTP-Mem in DMSO (**Fig. 1C**). Noticeably, the frontier orbital distribution confirms the TTP core design. The highest occupied molecular orbital (HOMO) is predominantly localized on the conjugated triphenylamine group, highlighting its electron-donating capabilities; the lowest unoccupied molecular orbital (LUMO) is predominantly localized on the electropositive pyridine salt moiety, highlighting its electron-accepting capabilities. Moreover, the overlap between the HOMO and LUMO orbitals at the thiophene group also highlights its role as a π-bridge between the two orbitals.

Time-Density Dependent Functional Theory (TD-DFT) calculations were then performed to extract the vertical excitation energy for the $S_0 \rightarrow S_1$ transition: ΔE = 2.827 eV (438.51 nm, f = 1.68) (**Fig. 1C**). Importantly, this high oscillator strength (f = 1.68) indicates a strongly allowed electronic transition, confirming the designed Intramolecular Charge Transfer (ICT) mechanism. Furthermore, the $S_0 \rightarrow S_1$ transition is dominated (coefficient = 0.60816) by the HOMO → LUMO transition (HOMO = -0.23471 Ha, LUMO = -0.07839 Ha, gap = 4.2537 eV) with minor contributions from the HOMO-1 → LUMO (HOMO-1 = -0.27125 HA, gap = 5.2292 eV, coefficient = -0.30658) and HOMO → LUMO+1 (LUMO + 1 = -0.02289, gap = 5.7433 eV, coefficient = 0.15700) transitions. Particularly, the discrepancy between the TD-DFT calculated value of 2.827 eV and the Kohn-Sham-eigenvalues-derived HOMO-LUMO gap reveals the presence of other transitions absent from the simple frontier orbital gap calculation.

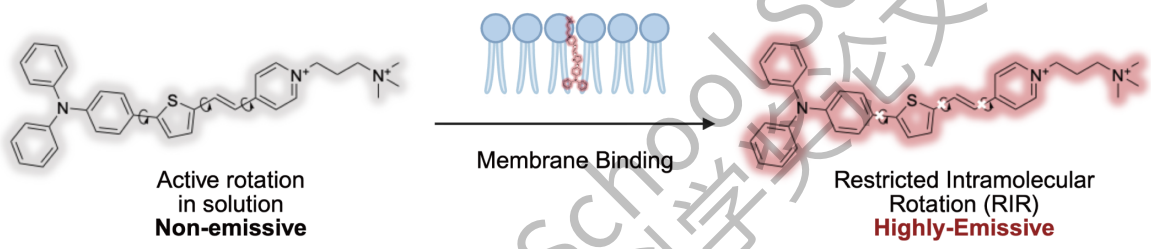
2.2.2 UV-Vis Absorption and Photoluminescence Spectroscopy Reveals AIE Properties of TTP-Mem

The photophysical characteristics of TTP-Mem was further characterized via UV-Vis absorption spectra and the photoluminescence (fluorescent) spectra. Specifically, TTP-Mem has a maximum absorption peak (λabs) at 484 nm, 481 nm, and 476 nm in DMSO, 90% Toluene/DMSO (v/v), and 99% PBS/DMSO (v/v), respectively (**Fig. 1D**). The lack of significant difference between the maximum absorption peaks can be attributable to the nature of absorption as a ground-state phenomenon (**Scheme 4**). In other words, absorption

2026 S.T. Yau High School Science Award
仅用于2026日成绩中学科学奖论文公开

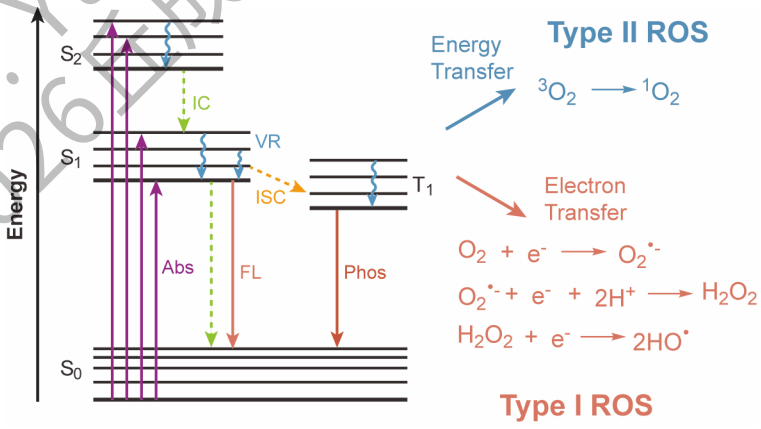
primarily reflects the ground-state geometry and electronic structure of the molecule because it consists of multiple Franck-Condon transitions from S_0 to various S_1 vibrational states (**Scheme 4**). Accordingly, the minimal difference in maximum absorption highlighted by the UV-Vis spectrum is indicative that the ground-state geometry and electronic structure of TTP-Mem remained largely unperturbed, regardless of aggregation states (**Fig. 1D**).

However, in aggregation, the excited state geometry and electronic structure of TTP-Mem changes significantly. Photoluminescence spectroscopy reveals that with increasing Toluene (poor solvent) concentrations, TTP-Mem relative emission intensities (I/I_0, normalized to maximum emission in pure DMSO) increased 29-fold (0% to 90% Toluene), indicative of strong AIE properties as TTP-Mem begin to cluster (**Fig. 1E-F**). This can be explained with Restricted Intramolecular Rotation (RIR), where the restriction of peripheral single-bond rotation in aggregate state suppresses non-radiative decay and allows the excited state energy to be released radiatively instead, leading to enhanced fluorescence. Similarly, TTP-Mem exhibits bright fluorescence when bound in parasite membrane (**Scheme 3**).



Scheme 3 | Schematic diagram illustrating the proposed RIR-activated emission of TTP-Mem bound to the inter-lipid space of the membrane. TTP-Mem is interlaced between the phospholipids of the membrane. Restricted rotation of its peripheral single bonds confers emissive-properties.

2.3 Electron Paramagnetic Resonance Spectroscopy and ABDA Probe Validates TTP-Mem Sonodynamic ROS Generation

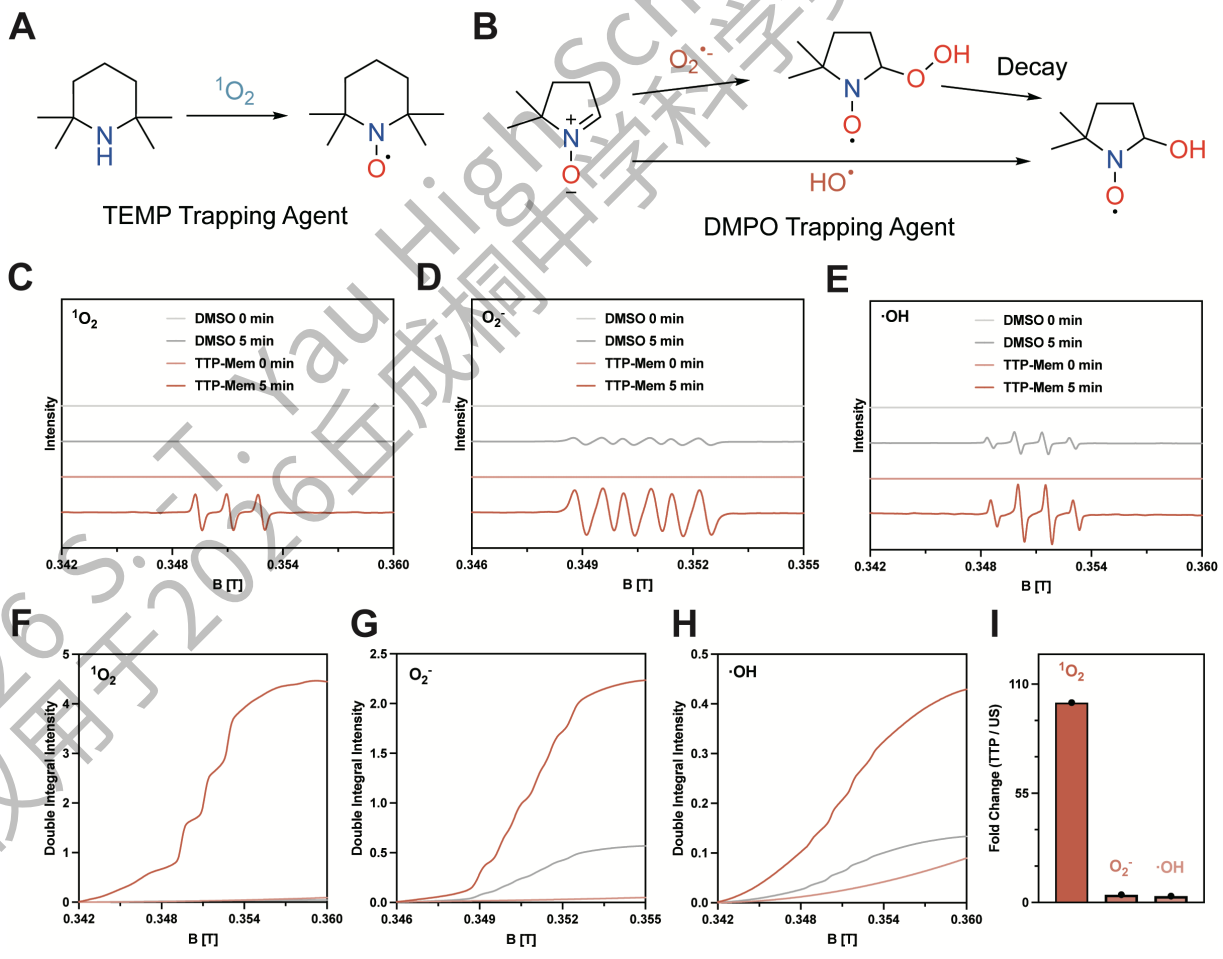


Scheme 4 | Schematic diagram illustrating the formation of Type I and Type II ROS from the Triplet Excited State after ISC. Jablonski diagram annotated with absorbance (Abs), fluorescence (FL), internal conversion (IC), vibrational relaxation (VR), intersystem crossing (ISC), and phosphorescence (Phos). The

2026 S.-T. Yau High School Science Award
仅用于2026丘成桐中学科学奖公示

two types of ROS are illustrated with their respective mechanisms, distinguishing Type I (electron transfer generating radical ROS) and Type II (energy transfer to ground-state oxygen generating singlet oxygen).

Having established the underlying RIR mechanism behind TTP-Mem's emissive characteristics when bound in membrane, we next investigated whether this excited-state stabilization could be leveraged for therapeutic functions through Reactive Oxygen Species (ROS) generation. ROS has been proven to cause significant damage to fundamental building blocks of the cell, including DNA, proteins, and importantly, lipids [17]. Noticeably, singlet excited states typically only exist for nanoseconds, which makes them especially hard to utilize for prolonged ROS generation [12], [46]. Instead, many AIE-active photosensitizers and sonosensitizers have been known to redirect singlet excited-state energy by way of intersystem crossing (ISC) into the triplet state, as shown in **Scheme 4**, where the spin-forbidden nature of the $T_1 \rightarrow S_0$ transition creates phosphorescence emissions with longer lifetimes (typically lasting microseconds to hundreds of milliseconds), making them easier to utilize for ROS generation [12], [46]. Moreover, ISC is especially favored in cases where non-radiative decay pathways are suppressed, such as in the case of TTP-Mem's RIR [12], inducing strong ROS generation. In general, ROS can be categorized into two types based on two different mechanisms: Type I R OS and Type II ROS (**Scheme 4**). Type I ROS, such as superoxide anion ($O_2^{-\bullet}$) and hydroxyl radical (•OH) are formed via electron transfer from the triplet state, while Type II ROS, singlet oxygen ($^1O_2$), is predominantly generated via energy transfer from the triplet state (**Scheme 4**) [12], [16].



2026 S.-T. Yau High School Science Award
仅用于2026丘成桐中学科学奖公示

Fig. 2 | Type I/II ROS yields of TTP-Mem under ultrasound-activation. (**A-B**) Schematic diagram illustrating the mechanism behind different trapping agents: TEMP (2,2,6,6-tetramethylpiperidine) reacts with singlet oxygen to form TEMPO (2,2,6,6-tetramethylpiperidine-1-oxyl) (**A**); DMPO (5,5-dimethyl-1-pyrroline N-oxide) reacts with hydroxyl radical to form DMPO-OH (2-hydroxy-5,5-dimethyl-1-pyrrolidinyloxy) and with superoxide anion to form DMPO-OOH paramagnetic adduct, which typically decays to DMPO-OH (**B**). **(C-E)** Electron paramagnetic resonance (EPR) spectra of TTP-Mem (5 μM) or DMSO alone, with or without 5 min of ultrasound activation (1.5w/cm^2, 50% duty cycle), using TEMP probe ($^1O_2$) **(C)**, DMPO probe in MeOH (O_2•$^-$) **(D)**, and DMPO probe in H_2O (•OH) **(E)**. **(F-H)** Double integral of EPR signals from **(C-E)**, respectively, quantifying relative ROS yields. **(I)** Calculated fold changes in maximum double integral EPR signal intensity between TTP-Mem and DMSO alone, each under 5 min ultrasound (1.5w/cm^2, 50% duty cycle).

Given the demonstrated aggregation-responsive photophysical property of TTP-Mem, and its photodynamic ROS generation efficacy established in a concurrent study (manuscript under revision), we sought to determine whether analogous excitation under ultrasound would confer the same ROS generation. To this end, electron paramagnetic resonance (EPR) spectroscopy, coupled with the ABDA (9,10-Anthracenediyl-bis(methylene)dimalonic acid) absorption probe assay, was used to characterize TTP-Mem ROS generation under sonodynamic activation.

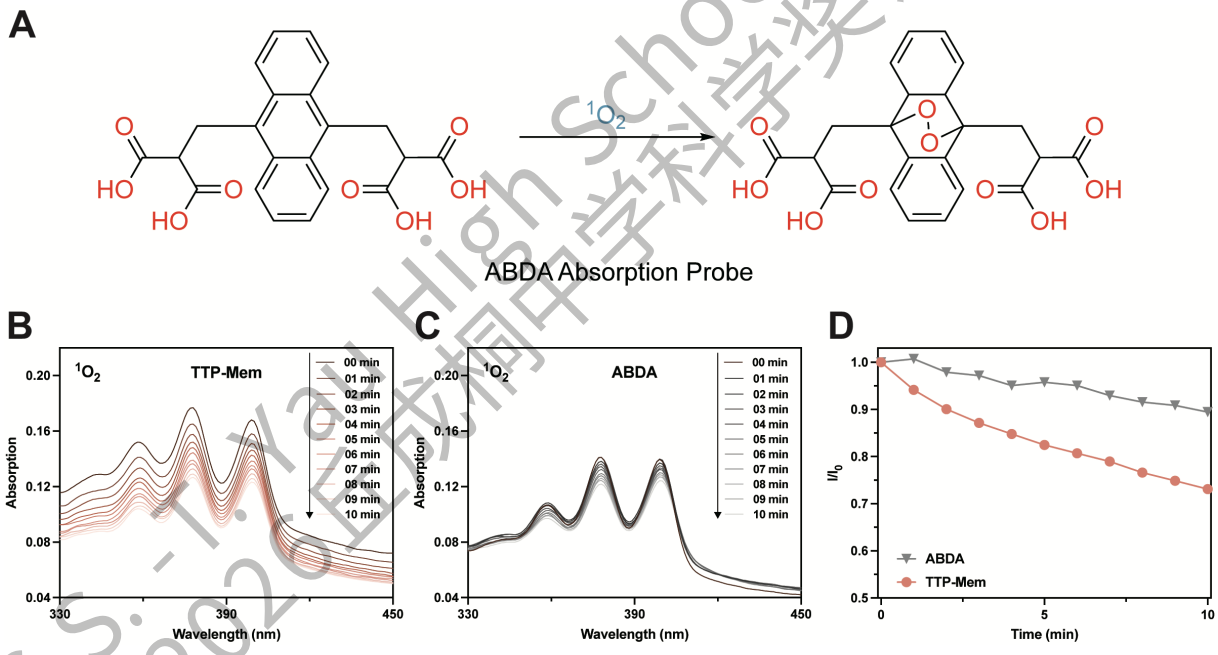


Fig. 3 | Time-course singlet oxygen ROS detection via ABDA absorption-based probe. (**A**) Schematic diagram illustrating ABDA (9,10-Anthracenediyl-bis(methylene)dimalonic acid) reacting with singlet oxygen to produce ABDA endoperoxide. **(B-C)** UV-Vis absorption spectra of ABDA probe (detects $^1O_2$) with TTP-Mem (5 μM) **(B)** or PBS alone **(C)** at increasing ultrasound activation times (0-10 min, 1.5w/cm^2, 50% duty cycle). (**D**) Plot of maximum absorption (λ=400 nm) and relative absorption intensity (I/I$_0$) versus activation time, a picture of TTP-Mem in 90% Toluene vs. 100% DMSO under ultraviolet irradiation is overlayed on top.

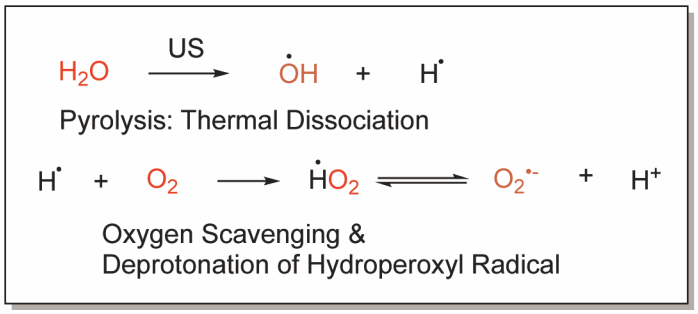
2026 S.-T. Yau High School Science Award 仅用于2026丘成桐中学科学奖论文公示

Since different ROS react preferentially with differentially spin-trapping agents, a panel of spin-trapping probes were utilized to comprehensively map TTP-Mem's ROS generation profile (**Fig. 2**). TEMP was used to characterize singlet oxygen ($^1O_2$), since it selectively oxidizes into TEMPO, a free radical detectable via EPR (**Fig. 2A**). DMPO was used to characterize both hydroxyl radicals (•OH) and superoxide anions ($O_2^{\bullet-}$), albeit in different systems. Specifically, the reaction between DMPO and superoxide anions form the unstable DMPO-OOH paramagnetic adduct, which decays to DMPO-OH, the product of DMPO and hydroxyl radicals, in water (**Fig. 2B**). To mitigate this, superoxide anion detection was conducted in methanol, while hydroxyl radical detection was conducted in water, separating the characterization of the two radicals. TEMPO, DMPO-OH, and DMPO-OOH are all detectable via EPR because the radical, unpaired electron on oxygen is delocalized over both N and O by occupying the π* antibonding orbital. Finally, ABDA was used as an absorption-based probe that reacts irreversibly with singlet oxygen to form an endoperoxide, resulting in a measurable decrease in absorbance that corresponds to cumulative $^1O_2$ generation over time (**Fig. 3**).

EPR spectra results reveal that TTP-Mem under sonodynamic activation is most capable at generating Type II ROS ($^1O_2$) and comparatively less capable at generating Type I ROS ($O_2^{\bullet-}$ and •OH) (**Fig. 2F-H**). In EPR, each nucleus with spin S is split into $2S + 1$ lines [47], [48]. TEMPO produces a 1:1:1 spectrum as nitrogen has a spin quantum number (S) of 1, splitting $2S + 1 = 3$ times (**Fig. 2C**) [49]. DMPO-OOH is first split 1:1:1 by nitrogen, spaced α_N apart, followed by a split caused by the proton ($S = 1/2$) on the hydroxyl group, spaced α_H apart. This creates a 1:1:1:1:1:1 (6 total lines) spectrum with roughly equal intensity (**Fig. 2D**) [50]. Similarly, DMPO-OH produces a spectrum that is first split 1:1:1 by nitrogen, spaced α_N apart, followed by a split caused by the proton ($S = 1/2$) on the hydroxyl group, spaced α_H apart. However, as $\alpha_N \approx \alpha_H$, DMPO-OH creates 1:2:2:1 splitting (**Fig. 2E**) [50], [51].

To quantitatively analyze ROS generation by TTP-Mem under sonodynamic activation, we further analyzed the double integral of EPR intensities (**Fig. 2F-H**; see Section 3.3). Noticeably, singlet oxygen double integral intensity increased over 100-fold when compared to DMSO under 5 min of ultrasound (**Fig. 2I**). Superoxide anion and hydroxyl radical fold changes were considerably lower, at 3.923 and 3.217 respectively (**Fig. 2I**).

Singlet oxygen generation was further characterized with the ABDA absorption-based probe under varying ultrasound irradiation times. The ABDA absorption time-course results indicate a near halved absorption-level (0 to 10 min) that demonstrates strong singlet oxygen generation capabilities by TTP-Mem under ultrasound irradiation (**Fig. 3B-D**). Therefore, TTP-Mem can be characterized as a predominantly Type II sonosensitizer, with significant singlet oxygen generation capabilities and comparatively less Type I generation capabilities.



2026 S.T. Yau High School Science Award
仅用于2026日成杯科学奖论文评

Scheme 5 | Schematic diagram illustrating the formation of Type I ROS from ultrasound-induced pyrolysis and subsequent secondary reactions. Mechanism adapted from [52], [53], [54], [55].

However, it should be noted that ultrasound irradiation alone is capable of producing massive amounts of Type I ROS independent of TTP-Mem, with prior studies demonstrating the capability of ultrasound-induced cavitation in generating hydroperoxyl radical, hydrogen peroxide, and superoxide anion [52], [53], [54], [56], [57], [58]. Noticeably, superoxide anion has been noted as one of the most abundant active oxygen species generated, matching our EPR results (**Fig. 2F**) [58]. Mechanistically, ultrasound irradiation induces rapid collapse and implosion of cavitation bubbles, which creates extreme local temperature and pressure that contribute to the thermal dissociation of water into hydroxyl (•OH) and hydrogen (•H) radicals (**Scheme 5**) [54]. Hydrogen radicals participate in subsequent secondary reactions, forming hydroperoxyl radicals (HO_2•) when reacted with dissolved molecular oxygen (**Scheme 5**) [53]. Finally, hydroperoxyl radicals (HO_2•) can deprotonate moderately (pKa = 4.8) into superoxide anion ($O_2^{\bullet-}$) (**Scheme 5**) [52], [55]. This equilibrium, among other subsequent reactions, allow ultrasound-induced cavitation to produce a Type I ROS pool independent of any sonosensitizer (**Fig. 2G-H**). In light of this view, with TTP-Mem as a sonosensitizer that predominantly generates Type II ROS, ultrasound may serve as a complimentary, TTP-Mem independent source of Type I ROS, providing increased ROS generation and a broader profile that may potentially compensate for TTP-Mem's comparatively weaker Type I generation.

2.4 Sonodynamic Activation Enhances TTP-Mem-Induced Membrane Disruption

2.4.1 Molecular Dynamics Simulation Elucidates TTP-Mem Preferred Bound Depth and Free Energy Profile

To understand TTP-Mem's membrane anchoring capabilities, steered molecular dynamics (SMD) was used to insert the ligand into the membrane along the bilayer normal while maintaining a near-upright orientation (**Fig. 4D**). From the final SMD position, restrained (10 ns) and unrestrained run (10 ns) were computed to determine TTP-Mem's general preferred bound depth (**Fig. 4C**): released from the imposed 0.73 nm in the restrained run, the center-of-mass (COM) differences increased significantly during the unrestrained free run, with TTP-Mem fluctuating at around 1.2 nm from the membrane center (**Fig. 4C**). Here, umbrella-sampling was used together with the weighted histogram analysis method (WHAM) to elucidate the potential of mean force (PMF) profile for the binding pocket (**Fig. 4B**). The umbrella PMF results are consistent with the picture revealed by the unrestrained run, with a single board well spanning ~1.3-1.8 nm that is largely flat (**Fig. 4B**). These results suggest that TTP-Mem binds at a preferred depth of around 1.5 nm. Crucially, the umbrella sampling PMF profile reveals an exhibit barrier of around 11 kJ/mol at ~2.2 nm. Taken together with the lack of escape observed in the unrestrained run, these MD runs establish TTP-Mem as kinetically locked in its membrane-bound state, consistent with the designed membrane-anchoring function.

Moreover, in the unrestrained MD run, no full flip along the ligand's primary axis (vertical axis) was observed. This highlights the efficacy of the designed lipophilic structure of the ligand, with its triphenylamine (TPA) core serving as a hydrophobic center that interacts favorably with the fatty acid tails of phospholipids and its pyridinium salt moiety serving as a hydrophilic center that interacts favorably with the phosphate heads of the phospholipids.

2026 S.T. Yau High School Science Award
仅用于2026丘成桐中学科学奖论文公开

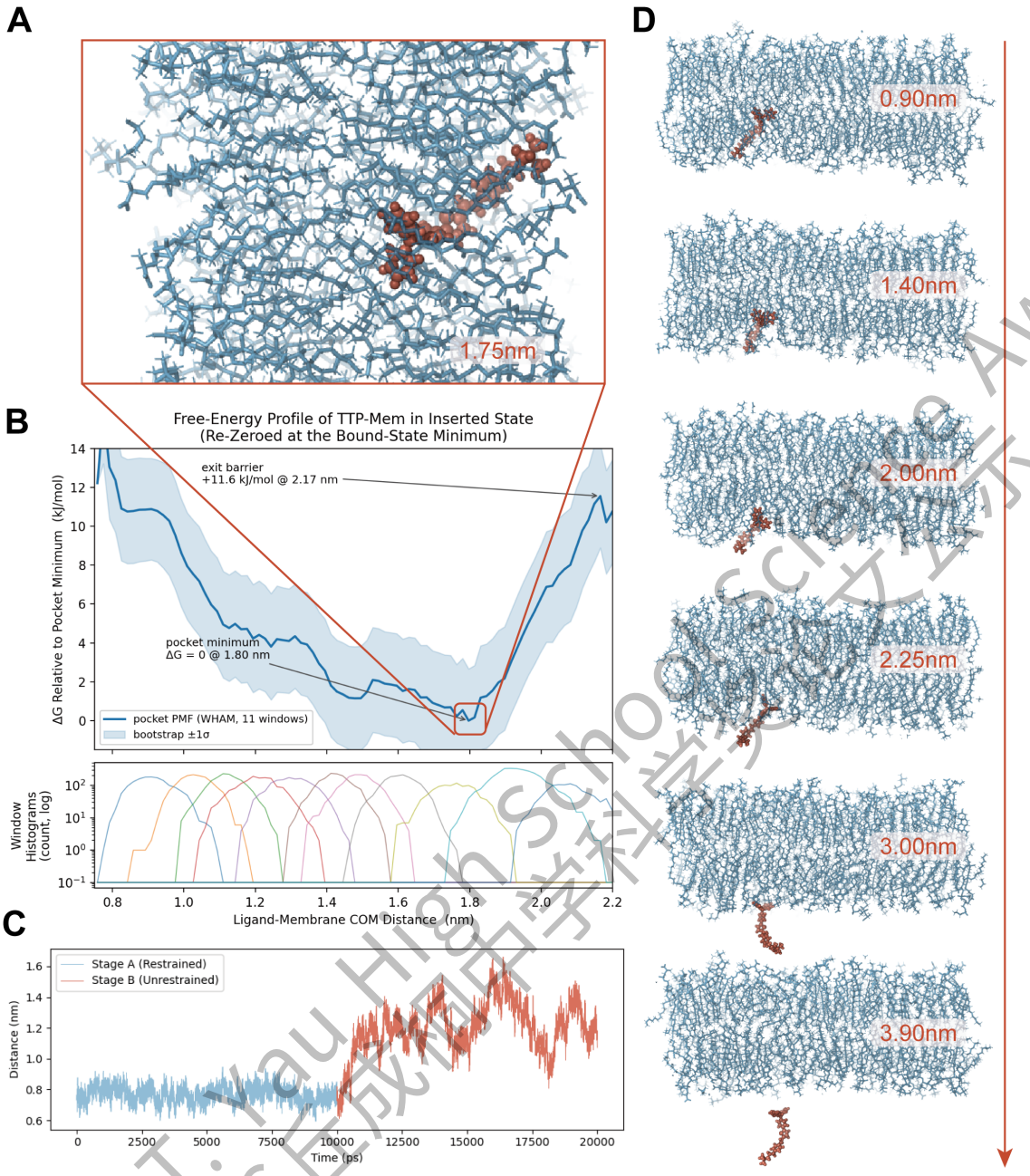


Fig. 4 | Molecular dynamics simulations reveal TTP-Mem's binding with the cell membrane. (**A**) Pocket minimum inserted state of TTP-Mem within the membrane, observed at close to 1.80 nm from the membrane center. (**B**) The potential of mean force (PMF) profile for TTP-Mem derived from weighted histogram analysis method (WHAM) of 11 umbrella sampling windows. (**C**) The vertical center-of-mass (COM) fluctuations of TTP-Mem during restrained and unrestrained molecular dynamic runs, extracted from the final positions of SMD runs. (**D**) An overview of the steered molecular dynamics (SMD) runs, labeled with different ligand-membrane COM distances.

2.4.2 Confocal Microscopy Reveals TTP-Mem Localization to the Parasitic Membrane

Given the high ligand-membrane affinity identified through steered molecular dynamics simulations, the localization of TTP-Mem to the parasitic membrane was verified experimentally with confocal microscopy.

2026 S.-T. Yau High School Science Award
仅用于2026丘成桐科学奖公示

Specifically, *T. gondii* tachyzoites were stained with DiIC12, an orange fluorescent probe that binds to the membrane, and ER-Tracker, an orange fluorescent probe that instead binds to the endoplasmic reticulum (**Fig. 5A-B**). Colocalization results confirm the binding of TTP-Mem to the parasitic membrane, with a calculated Pearson correlation coefficient (R) of 0.78 ($P < 0.0001$) between the DiIC12 fluorescent channel and the TTP-Mem fluorescent channel (**Fig. 5C**); conversely, there were no significant correlation between the ER-Tracker fluorescent channel and the TTP-Mem fluorescent channel ($P = 0.2859$, R = 0.08921) (**Fig. 5C**). The high correlation between TTP-Mem fluorescent channels and the DiIC12 membrane tracker verify the binding capability of TTP-Mem to *T. gondii* tachyzoites' membrane.

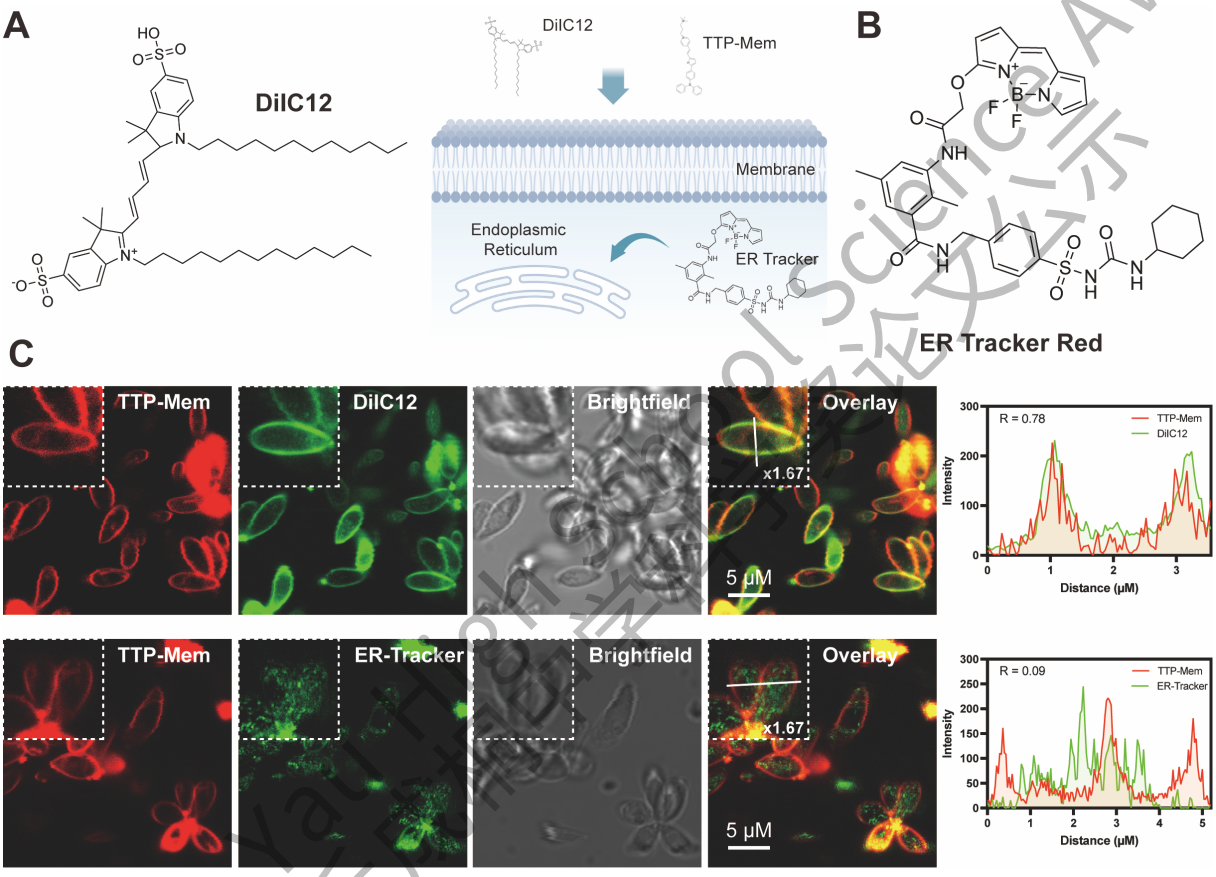


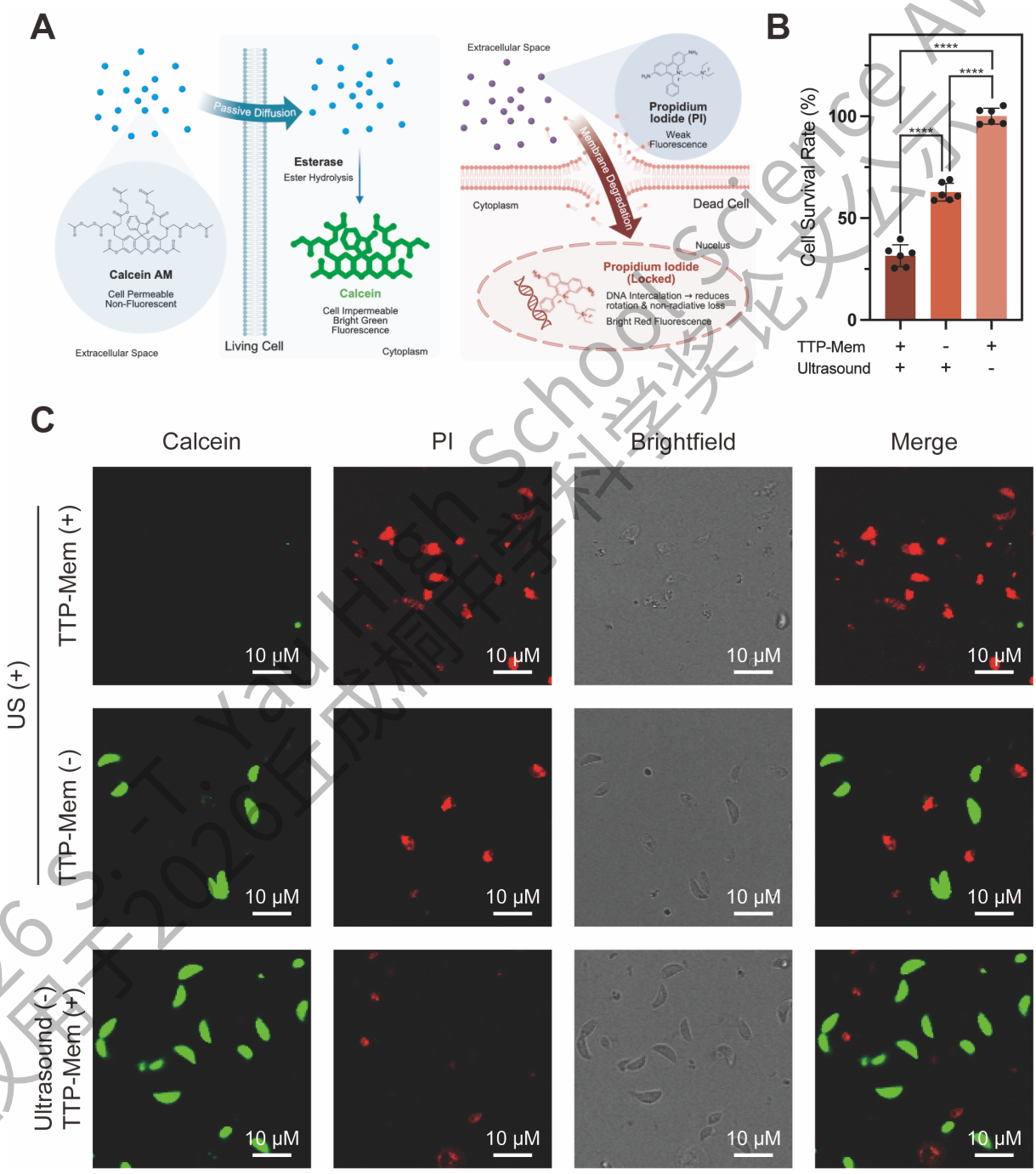
Fig. 5 | Organelle colocalization of TTP-Mem in *T. gondii* tachyzoites under confocal microscopy. (A-B) Skeletal structure of DiIC12 probe (**A**) and ER-Tracker probe (**B**) used to track *T. gondii* parasite membrane, with an illustration showing their binding locations. (**C**) Confocal images showing organelle colocalization of TTP-Mem (λex = 488 nm, λem = 650-750 nm) with DiIC12 (λex = 561 nm, λem = 560-650 nm) and ER-Tracker (λex = 561 nm, λem = 560-650 nm), with their respective correlation coefficients (R). Scale bar: 5 μm.

2.5 Ultrasound-Enhanced Rapid Membrane Disruption Introduces Near-Instantaneous Parasiticidal Death

2.5.1 Calcein/PI Staining Substantiates Ultrasound-Induced Membrane Dysfunction and Parasite Death

To quantitatively determine the efficacy of TTP-Mem Sonodynamic Therapy (SDT), Calcein-AM/PI (live/dead) staining was evaluated. Calcein AM is a cell-permeable, non-fluorescent probe that passively

diffuses through cellular membranes. Intracellular esterases subsequently hydrolyze Calcein-AM into Calcein through ester hydrolysis (**Fig. 6A**). Calcein is a cell-impermeable, bright green fluorescent probe that indicates cell vitality. On the contrary, Propidium Iodide (PI) can be used to characterized dead cells that have experienced membrane disruption. Specifically, PI displays weak fluorescence when in free solution due to the unrestricted rotation of its single bonds outcompeting radiative pathways. When membrane degradation occurs, it is able to enter the cell cytoplasm and interlace with the DNA. Here, DNA reduces the rotation of its single bonds and suppresses non-radiative loss, allowing PI to display a bright-red fluorescence (**Fig. 6A**).



2026 年 T. Yau High School Science Award 仅用于2026年成都市科学论文公示

Fig. 6 | Evaluation of TTP-Mem-SDT-induced killing of *T. gondii* tachyzoites assessed by Calcein-AM/PI (live/dead) staining. (A) Schematic diagram illustrating Calcein AM and Propidium Iodide (PI) fluorescent conditions and mechanisms. **(B)** Cell survival rate comparisons between TTP-Mem (5 μM) with ultrasound (1.5w/cm^2, 50% duty cycle, 3 min), ultrasound alone (1.5w/cm^2, 50% duty cycle, 3 min), and TTP-Mem alone (5 μM). Data presented with one-way Welch's ANOVA and Games-Howell post-hoc test, ****: $P < 0.0001$ and normalized to TTP-Mem alone. **(C)** Confocal images of TTP-Mem (λex = 488 nm, λem = 650-750 nm) with ultrasound, ultrasound alone, and TTP-Mem alone stained with Calcein (λex = 488 nm, λem = 500-540 nm) and PI (λex = 561 nm, λem = 590-640 nm). Scale bar: 10 μm.

Calcein-AM/PI confocal microscopy (**Fig. 6C**) illustrates the strong toxicity of TTP-Mem SDT in killing *T. gondii* tachyzoites. Indeed, while ultrasound alone was capable of killing nearly 60.97% of the *T. gondii* tachyzoites, this is significantly lower than the 80.4% efficacy of TTP-Mem SDT ($P < 0.0001$ one-way Welch's ANOVA with Games-Howell post-hoc test; **Fig. 6B**). This significant difference demonstrates that ultrasound-mediated sonodynamic activation significantly improves TTP-Mem's parasiticidal efficacy beyond what either ultrasound or TTP-Mem alone could achieve independently.

2.5.2 SOSG Probing Confirms Membrane-Proximal ROS Generation

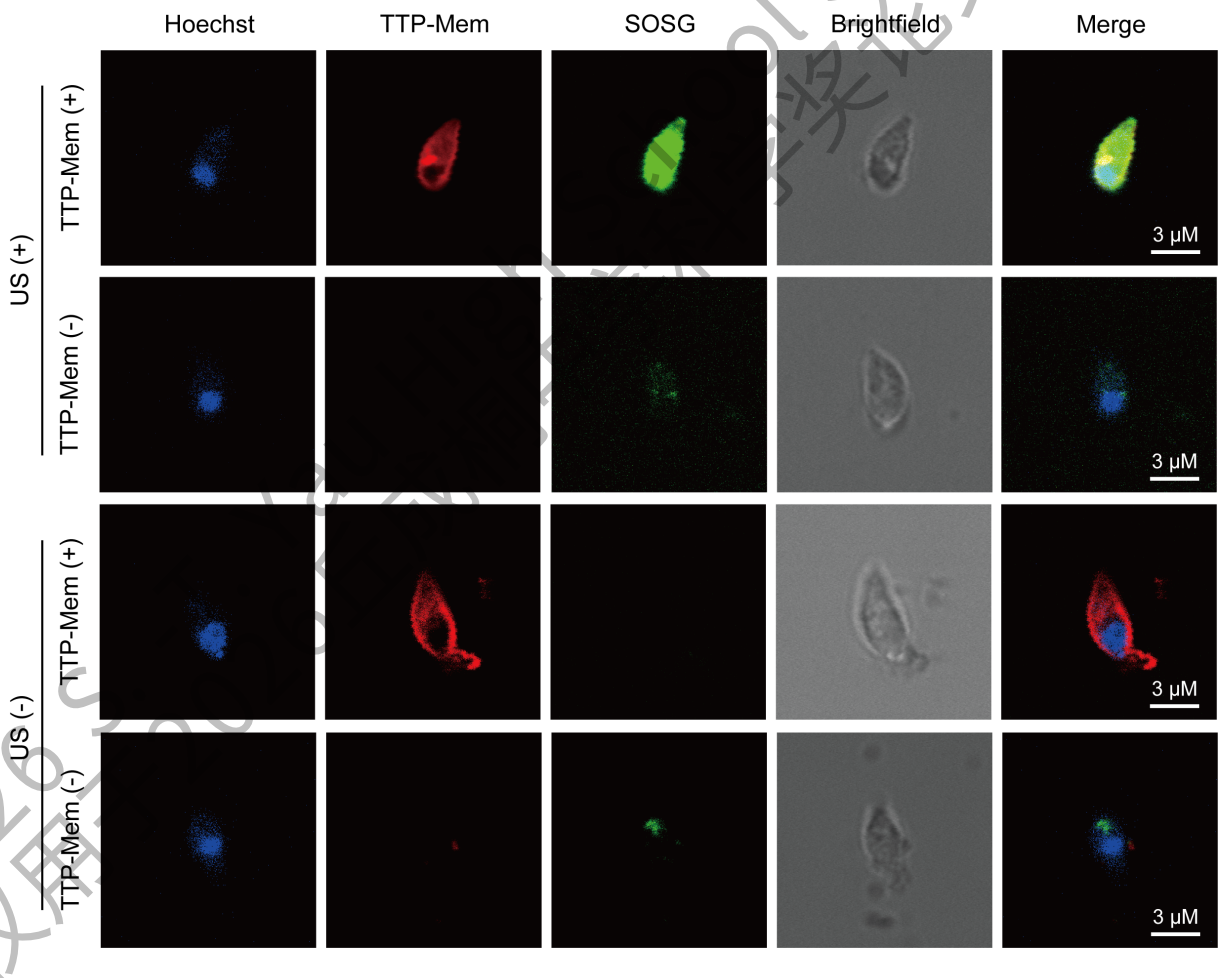


Fig. 7 | Type II membrane-proximal ROS generation in *T. gondii* tachyzoites under confocal microscopy. Confocal images of *T. gondii* tachyzoites stained with Hoechst (nucleus, λex = 405 nm, λem = 410-480 nm), Singlet Oxygen Sensor Green (SOSG, $^1O_2$, λex = 488 nm, λem = 500-550 nm) under four

conditions: with or without TTP-Mem (5μM, λex = 488 nm, λem = 650-750 nm), and with or without ultrasound (1.5w/cm^2, 50% duty cycle, 3 min). Scale bar: 3 μm.

Based on the previous ABDA absorption spectrum and EPR spectra that confirm TTP-Mem's Type II ROS generation under ultrasound irradiation (**Fig. 2-3**), we attempted to verify this production in vitro. To this end, singlet oxygen sensor green (SOSG) was used with Hoechst to stain *T. gondii* tachyzoites to characterize TTP-Mem Type II ROS generation. SOSG confocal microscopy results confirm the presence of strong singlet oxygen generation with TTP-Mem under ultrasound irradiation, significantly lower singlet oxygen generation with ultrasound alone, and close to no singlet oxygen generation in groups with no ultrasound (**Fig. 7**). This underscores the capability of TTP-Mem as a Type II sonosensitizer, highlighting its potential as an excellent candidate for sonodynamic therapy.

2.5.3 Scanning Electron Microscopy Elucidates Morphological Features of Structural Membrane Damage Post-SDT

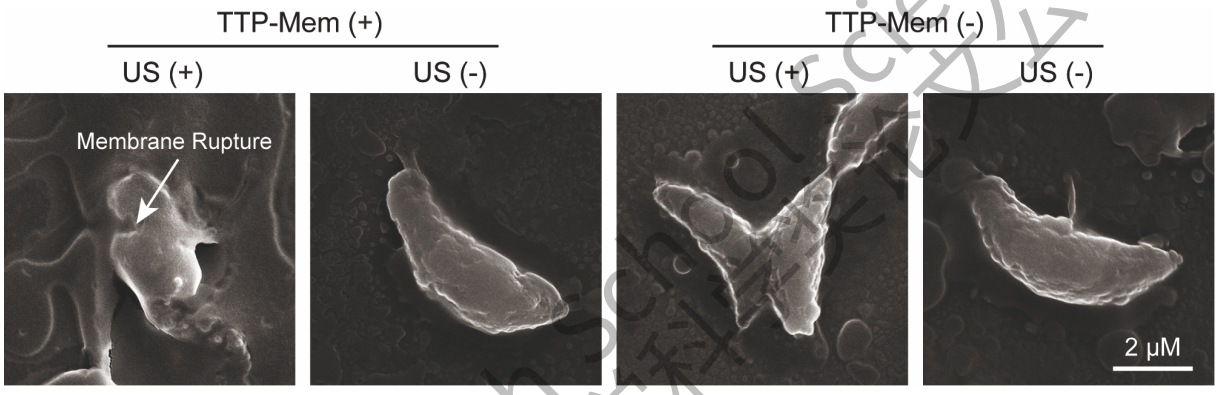
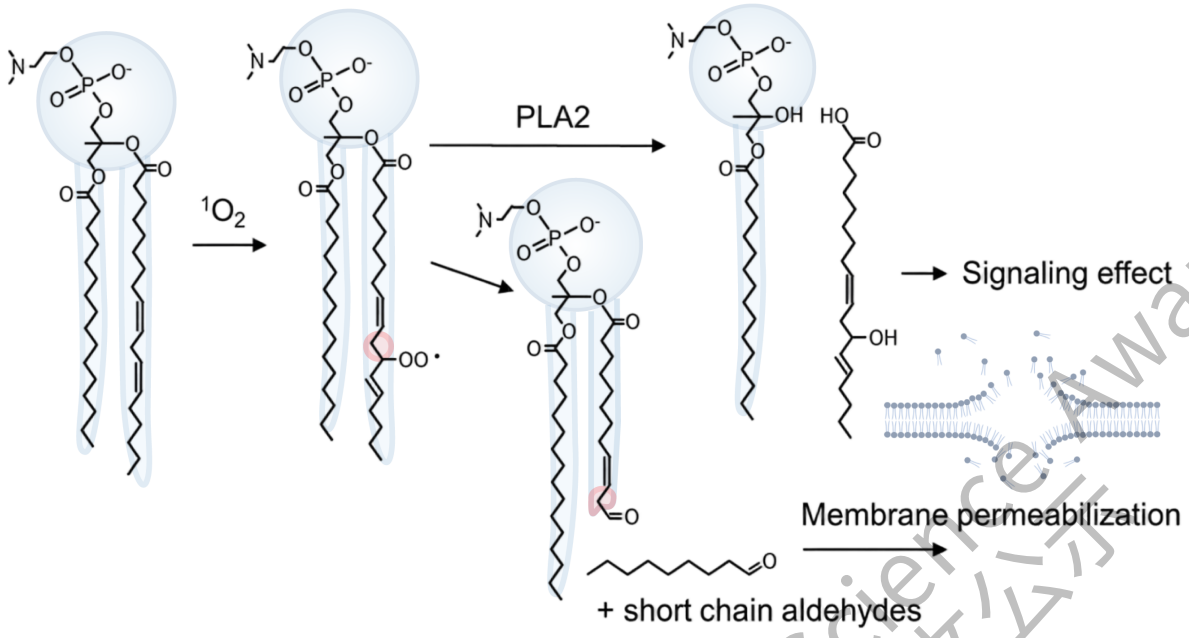


Fig. 8 | Scanning Electron Microscope images of *T. gondii* TTP-Mem-SDT-induced morphological damage. Scanning electron microscopy images of *T. gondii* morphology under four conditions: with or without TTP-Mem (5 μM), and with or without ultrasound (1.5w/cm^2, 50% duty cycle, 3 min). Membrane rupture is observed at TTP-Mem and ultrasound condition, indicative of membrane disruption. Scale bar: 2 μm.

Even though the killing efficacy of TTP-Mem SDT in killing *T. gondii* has been established through Calcein/PI staining, and its underlying mechanism elucidated through various ROS probes, the exact damage induced by TTP-Mem SDT remains unclear. To this end, scanning electron microscopy was used to characterize TTP-Mem SDT morphological damage. Scanning electron microscopy reveals that TTP-Mem under ultrasound-activation induces membrane rupture, a hallmark of membrane disruption. Specifically, under TTP-Mem SDT, *T. gondii* membrane structural integrity is lost, with severe membrane rupture and extrusion of cytoplasmic contents (**Fig. 8**). This highlights the efficacy of TTP-Mem as a sonosensitizer in causing swift parasitic membrane damage, consistent with the ROS-mediated killing mechanism (extreme singlet oxygen generation, complemented by ultrasound-induced Type I ROS) established through EPR, ABDA, and SOSG assays (**Fig. 2-3**, **7**).

2026 S.T. Yau High School Science Award 仅用于2026丘成桐中学科学奖公示



Scheme 6 | Schematic diagram illustrating the impact of singlet oxygen ROS on membrane fatty acids. Figure adapted and modified from [59] © 2023, licensed under CC BY 4.0.

Importantly, exposure to ROS can induce membrane permeation damage with the formation of lipid peroxyl radicals and lipid peroxide, the former further propagating oxidative chain reactions with other lipids (**Scheme 6**) [17], [59]. This highlights a potential mechanism in explaining the observed morphological damage in the SEM images.

2.6 In Vitro Crystal Violet Plaque Assay Corroborates Anti-Parasitic Efficacy of TTP-Mem SDT

Having established the efficacy of TTP-Mem SDT in inducing membrane rupture in *T. gondii* tachyzoites, subsequent analysis involved evaluating whether TTP-Mem SDT translated to real efficacy in reducing parasite viability and infectivity. To this end, in vitro crystal violet plaque assay was employed to assess the anti-parasitic efficacy of TTP-Mem SDT, wherein reduced plaque formation reflects diminished parasite-induced cell lysis.

Specifically, we compared parasite-mediated plaque formation following treatment with a dark control group — TTP-Mem alone (5 μM), a positive control group — ultrasound alone (1.5w/cm^2, 50% duty cycle, 1.5 min), and experimental groups — TTP-Mem SDT at increasing concentrations (5 μM, 15 μM, 45 μM). Noticeably, ultrasound irradiation time was shortened to 1.5 min compared to other studies to highlight the short duration necessary to induced significant damage on *T. gondii*. While ultrasound irradiation alone noticeably decreased plaque formation relative to the dark control, TTP-Mem SDT markedly enhanced this inhibitory effect, resulting in significant suppression in macroscopic plaque areas (**Fig. 9A**). Furthermore, this inhibitory effect is clearly concentration-dependent, with increasing concentrations of TTP-Mem under fixed ultrasound irradiation parameters progressively suppressing plaque area formation (**Fig. 9B**).

Quantitative analysis through ImageJ confirmed that ultrasound alone reduced plaque area by 77% (relative to control), accentuated by TTP-Mem SDT, which boosted reduction levels to 84.3%. At escalating TTP-

2026 S.-T. Yau High School Science Award
仅用于2026丘成桐中学科学奖论文公开

Mem concentrations, near total eradication of TTP-Mem was achieved, with plaque area reductions reaching 96.3% at 15 μM and 99.86% at 45 μM (**Fig. 9C**). Collectively, these findings highlight the potential of TTP-Mem as a membrane-targeting sonosensitizer in potent suppression of *T. gondii* parasites, dramatically curtailing *T. gondii* viability, infectivity, and intracellular proliferation.

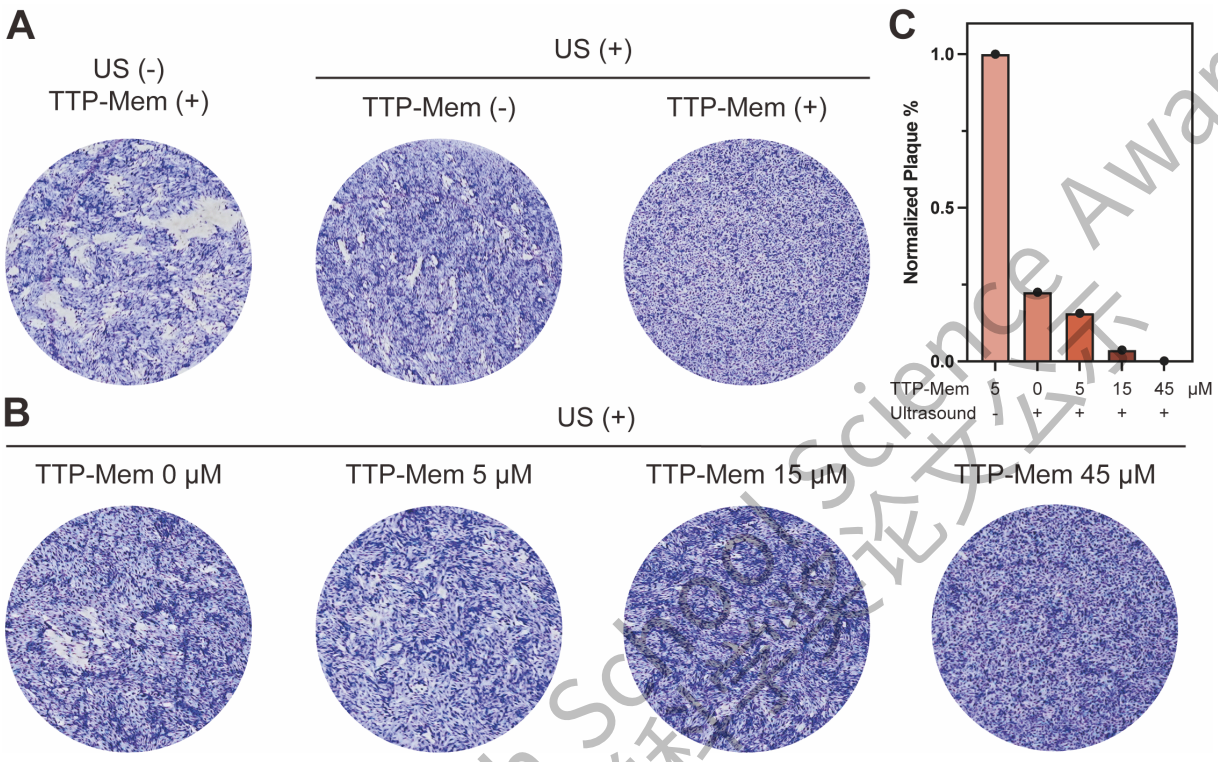


Fig. 9 | Crystal violet plaque assay of anti-*T. gondii* efficacy of TTP-Mem SDT. (A) Crystal violet plaque assay of TTP-Mem (5 μM) alone, ultrasound (1.5w/cm^2, 50% duty cycle, 1.5 min) alone, and TTP-Mem (5 μM) with ultrasound (1.5w/cm^2, 50% duty cycle, 1.5 min). **(B)** Crystal violet plaque assay of increasing TTP-Mem concentrations (0 μM, 5 μM, 15 μM, and 45 μM) under ultrasound activation. (**C**) Plaque area percentages under varying concentrations of TTP-Mem (0 μM, 5 μM, 15 μM, 45 μM) SDT (1.5w/cm^2, 50% duty cycle, 1.5 min), normalized to the control group (5 μM TTP-Mem, no ultrasound).

3. Materials & Methodology

3.1 TTP-Mem Synthesis and Structural Verification

3.1.1 Synthesis of Compound C

In a 50 mL single-neck, round-bottom flask equipped with a magnetic stirrer and a Liebig condenser, a mixture of 400 μL 4-methylpyridine (**Compound A**, CAS: 108-89-4, 382.8 mg, ρ = 0.957 g/mL) and 3-bromo-N,N,N-trimethylpropan-1-aminium bromide (**Compound B**, CAS: 3779-42-8, 1.0024 g) dissolved in N,N-Dimethylformamide (DMF, 5 mL) was stirred and heated at 100°C for 2 hours. After cooling to room temperature, the components were concentrated via rotary evaporation at 50 °C under reduced pressure to yield 4-methyl-1-(3-(trimethylammonio)propyl)pyridin-1-ium (**Compound C**) as a viscous, orange residue

2026 S.T. Yau High School Science Award 仅用于2026丘成桐中学科学奖论文公示

(**Fig. 10**). Due to the water-sensitive nature of the pyridinium salt, the intermediate was immediately transferred to the next step without further purification.

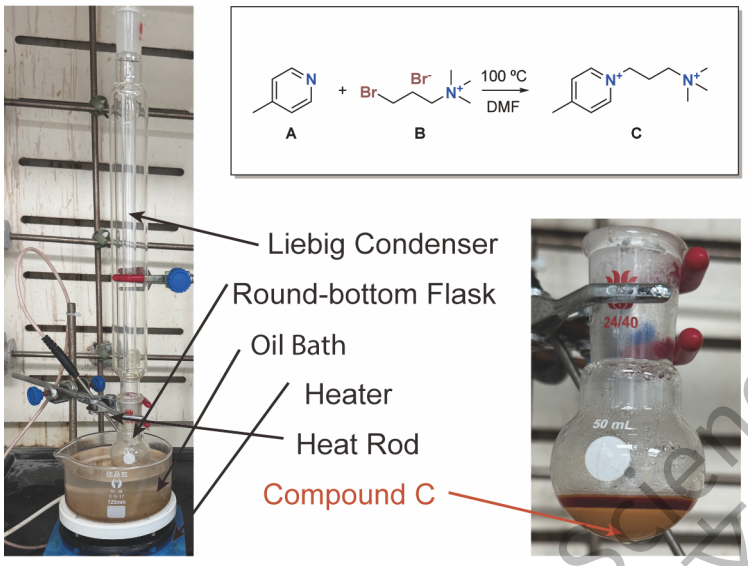


Fig. 10 | Synthesis of Compound C from reaction between Compound A and Compound B. Photographs detailing the used reflux apparatus setup annotated with different components (left), reaction overview (top), and reaction product (right).

3.1.2 Synthesis of TTP-Mem

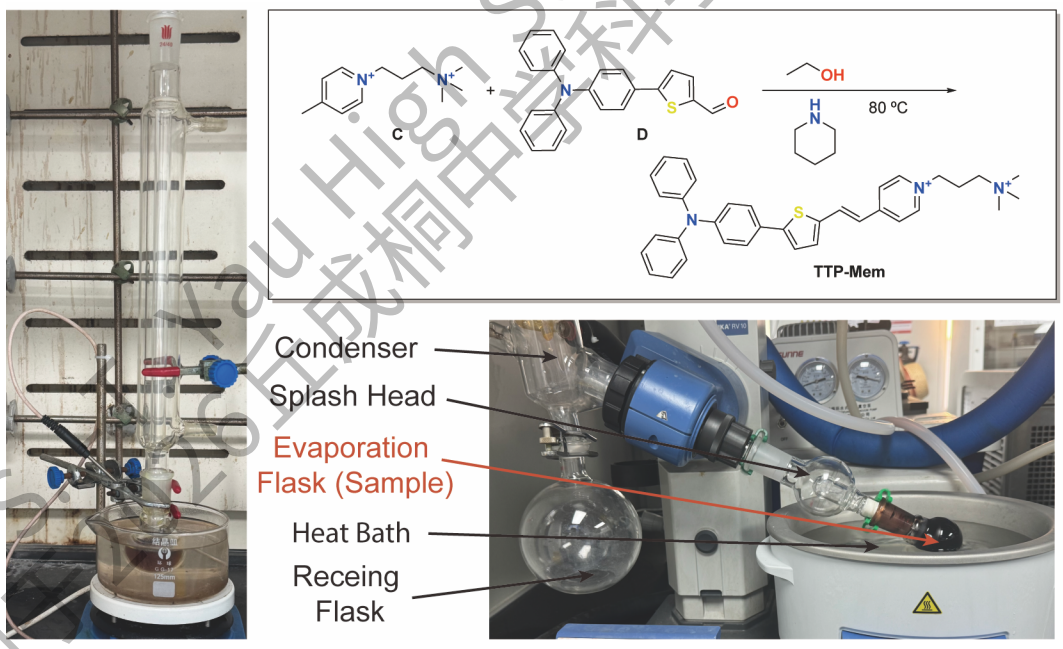


Fig. 11 | Synthesis of TTP-Mem from reaction between Compound C and Compound D. Photographs detailing the used reflux apparatus setup used to synthesis TTP-Mem (left), reaction overview (top), and the rotary evaporator used to afford the dark magenta product, annotated with individual components (right).

The obtained **Compound C** (1.0933 g) and 5-(4-(diphenylamino)phenyl)thiophene-2-carbaldehyde (**Compound D**, CAS: 291279-14-6, 1 g) were dissolved in anhydrous ethanol (15 mL) and piperidine (1 mL)

2026 Siyau High School Science Award 仅用于2026年思源杯科学论文公示

was then added as a base. The same setup was used and the reaction mixture was stirred under reflux at 80 °C for 24 hours (**Fig. 11**). Upon completion, the solvent was removed with rotary evaporation at 50 °C under reduced pressure for 1 hour, affording a dark maroon crude product (**Fig. 11**).

3.1.3 Purification of TTP-Mem

For purification, the dark maroon product was redissolved in dichloromethane (DCM) and methanol (MeOH) and transferred to a 100 mL round-bottom flask. Chromatographic neutral alumina (Al_2O_3) was then added to the solution to pre-absorb the sample. The resulting suspension was dried using rotary evaporation at 37 °C under reduced pressure until a free-flowing, homogenous power was obtained. The pre-absorbed neutral alumina powder was dry-loaded directly onto the head of the prepared chromatography column, and chromatographic separation was performed using a stepwise gradient elution of DCM/MeOH (100% DCM, 200:1, 100:1, 50:1, and 40:1, v/v) (**Fig. 12**). The resulting product was concentrated via rotary evaporation at 50 °C under reduced pressure. To further remove impurities, the residue was redissolved in minimal DCM and MeOH and recrystallized through the slow addition of excess n-Hexane under ultrasound agitation (**Fig. 12**). The resulting precipitate was isolated through vacuum filtration using a Büchner funnel. The dissolution, recrystallization, and filtration cycle was repeated 3 times to maximize purity.

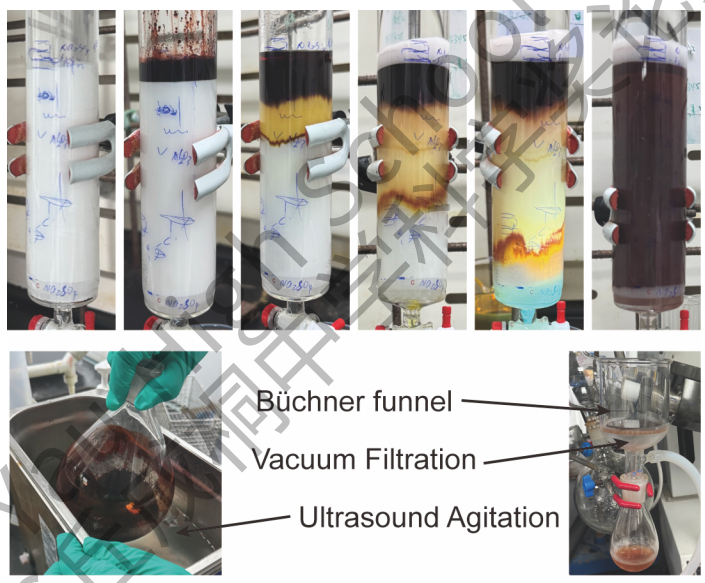


Fig. 12 | Initial purification workflow of TTP-Mem through column chromatography, dissolution, recrystallization, and vacuum filtration. Photograph of the neutral column showing the progressive migration and elution of the target bands (top), ultrasound-assisted anti-solvent recrystallization of TTP-Mem (DCM/n-Hexane) (left), and isolation of the purified precipitate via vacuum filtration through a Büchner funnel (right).

Due to the persistence of trace impurities, the precipitate was redissolved in DCM with minimal MeOH and purified with a short neutral alumina column (plug filtration) using DCM/MeOH (100% DCM, 100:1, 80:1, 70:1, 50:1, and 40:1) as the eluent (**Fig. 13**). The purified eluent was concentrated under reduced pressure at 50 °C. The dissolution, recrystallization, and filtration cycle was once more repeated with DCM and n-Hexane. To thoroughly eliminate remaining traces of non-deuterated solvents (remaining DCM, n-Hexane, and MeOH) that could interfere with subsequent NMR characterization, the purified product was redissolved

2026 S. T. Yau High School Science Award 仅用于2026丘成桐中学科学奖公示

in minimal deuterated methanol (CD_3OD) and frozen rapidly via immersion into liquid nitrogen (-196 °C) for several seconds, then evaporated under reduced pressures. The resulting TTP-Mem was obtained as a dark maroon solid and immediately submitted for structural verification.

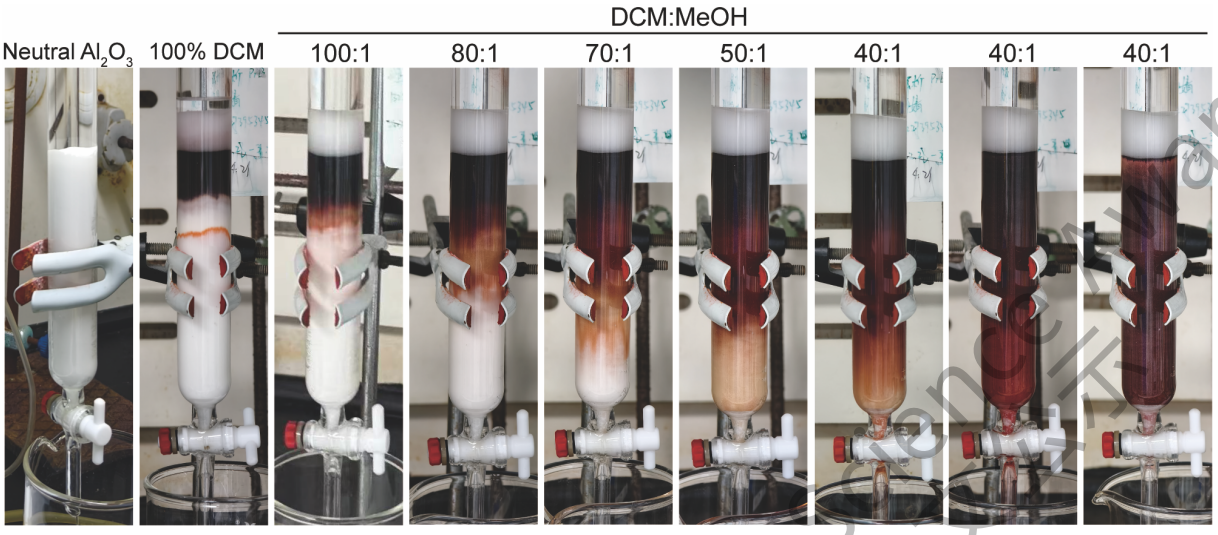
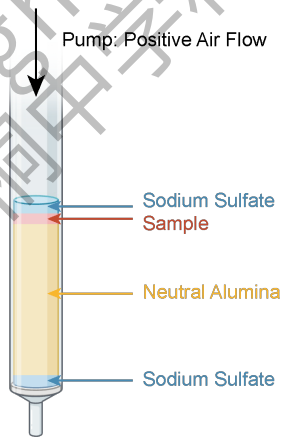


Fig. 13 | Second polish purification of TTP-Mem utilizing a short neutral alumina plug. Chromatographic separation and band separation observed on the neutral alumina plug during stepwise gradient elusion with DCM/MeOH (pure DCM to 40:1, v/v).

3.1.4 Preparation of Chromatography Column



Scheme 7 | Schematic diagram showing illustrating the components of the neutral alumina chromatography column. A layer of sodium sulfate is placed first, followed by the stationary phase, neutral alumina. The sample is placed on top of the neutral alumina column, which is covered with sodium sulfate to protect the absorbent bed.

A critical step in the purification of TTP-Mem involved the preparation of the neutral alumina chromatography column. The first fritted-disk neutral alumina chromatography column was prepared via several steps. First, a layer of anhydrous sodium sulfate (Na_2SO_4) was used at the bottom to provide bed stabilize and prevent fine stationary phase particles (neutral alumina) from escaping. Next, neutral alumina

2026 S.-T. Yau High School Science Award 仅用于2026丘成桐中学科学奖公示平台

was added to 1/3 of column height and tapped gently to compact the packing material. The columns were further compacted with DCM and positive air pressure to avoid channeling. This step is critical, since a uniformly compacted column bed is essential for high separation resolution. Finally, another layer of anhydrous sodium sulfate was added at the top of the sample to physically protect the absorbent bed from being disturbed by the fresh mobile phase poured at the top. The second plug filtration plain-bore neutral alumina column was prepared similarly, but with a preceding step: the standard glass column was fitted with a compacted cotton plug before the overlay of the anhydrous sodium sulfate layer to establish a flat, stable support bed. An illustration of the prepared chromatography can be found in **Scheme 7**.

3.1.5 TTP-Mem ^{1}H NMR Characterization

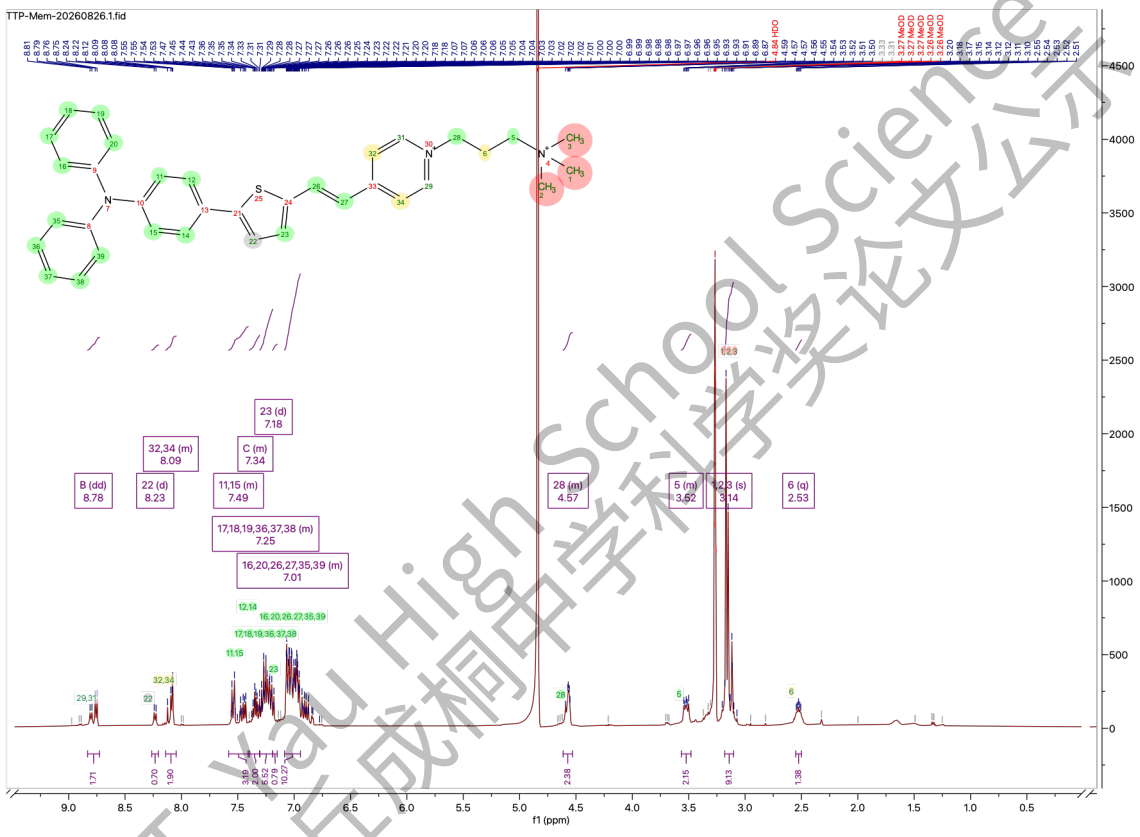


Fig. 14 | ^{1}H NMR of the purified TTP-Mem. Proton nuclear magnetic resonance spectrum of the synthesized and purified TTP-Mem. Spectrum of synthesized TTP-Mem annotated with chemical shifts, splitting patterns (multiplets), and peak assignments.

The purified TTP-Mem was verified through ^{1}H nuclear magnetic resonance (NMR) spectrum. The following information was obtained through manual assignment in MestReNova: 1H NMR (400 MHz, MeOD) δ 8.84 (dd, J = 18.2, 6.6 Hz, 2H), 8.30 (d, J = 6.6 Hz, 1H), 8.20 – 8.11 (m, 2H), 7.64 – 7.47 (m, 2H), 7.46 – 7.37 (m, 1H), 7.40 – 7.26 (m, 4H), 7.25 (dd, J = 7.4, 2.0 Hz, 1H), 7.15 – 6.82 (m, 9H), 4.68 – 4.59 (m, 2H), 3.63 – 3.54 (m, 2H), 3.29 – 3.11 (m, 9H), 2.59 (q, 1H), 1.72 (s, 1H).

3.1.6 TTP-Mem ^{13}C NMR Characterization

2026 S. T. Yau High School Science Award 仅用于2026丘成桐中学科学奖论文公示

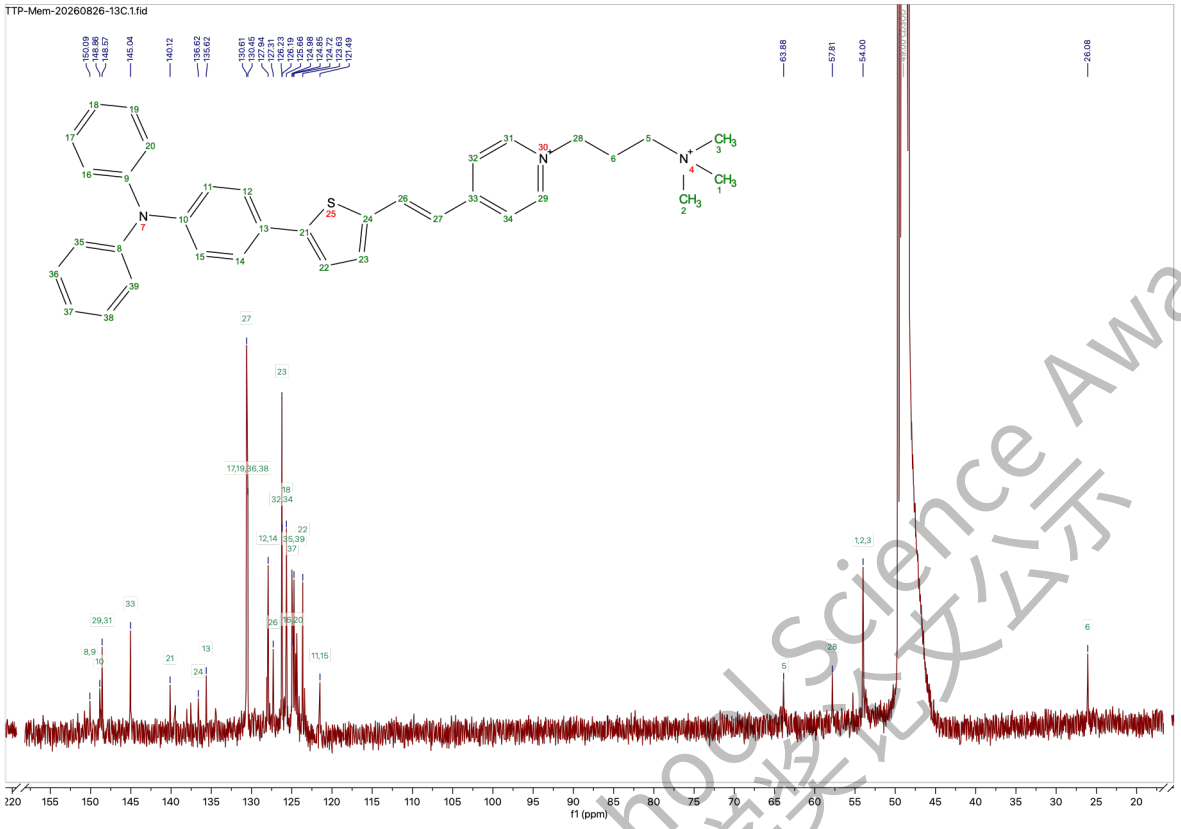


Fig. 15 | ^{1}H NMR of the purified TTP-Mem. Carbon-13 nuclear magnetic resonance spectrum of the synthesized and purified TTP-Mem. Spectrum of synthesized TTP-Mem annotated with chemical shifts and peak assignments.

The purified TTP-Mem was subsequently verified via ^{13}C nuclear magnetic resonance (NMR) spectrum. The following information was through manual assignment in MestReNova: 13C NMR (101 MHz, MeOD) δ 150.09 (C-8,9), 148.87 (C-10), 148.57 (C-29,31), 145.04 (C-33), 140.12 (C-21), 136.62 (C-24), 135.62 (C-13), 130.61 (C-27), 130.46 (C-17,19,36,38), 127.94 (C-12,14), 127.31 (C-26), 126.23 (C-23), 126.19 (C-32,34), 125.66 (C-18), 124.98 (C-37), 124.85 (C-16,20), 124.72 (C-35,39), 123.63 (C-22), 121.49 (C-11,15), 63.88 (C-5), 57.81 (C-28), 54.00 (C-1,2,3), 26.08 (C-6).

3.1.7 TTP-Mem High Resolution Mass-Spectroscopy Characterization

Next, the purified TTP-Mem was finally characterized through high resolution mass spectroscopy (TOF MS ES+: time-of-flight mass spectroscopy analyzer with electrospray ionization, positive mode). As shown in **Fig. 16**, the m/z peak 265.6366 was identified (calculated theoretical of 265.63486 from ChemDraw). Because TTP-Mem contains two positive charges, this corresponds to an exact mass of 531.2732, yielding a less than 0.004 difference from theoretical values.

2026 S. T. Yau High School Science Award 仅用于2026丘成桐中学科学奖公示

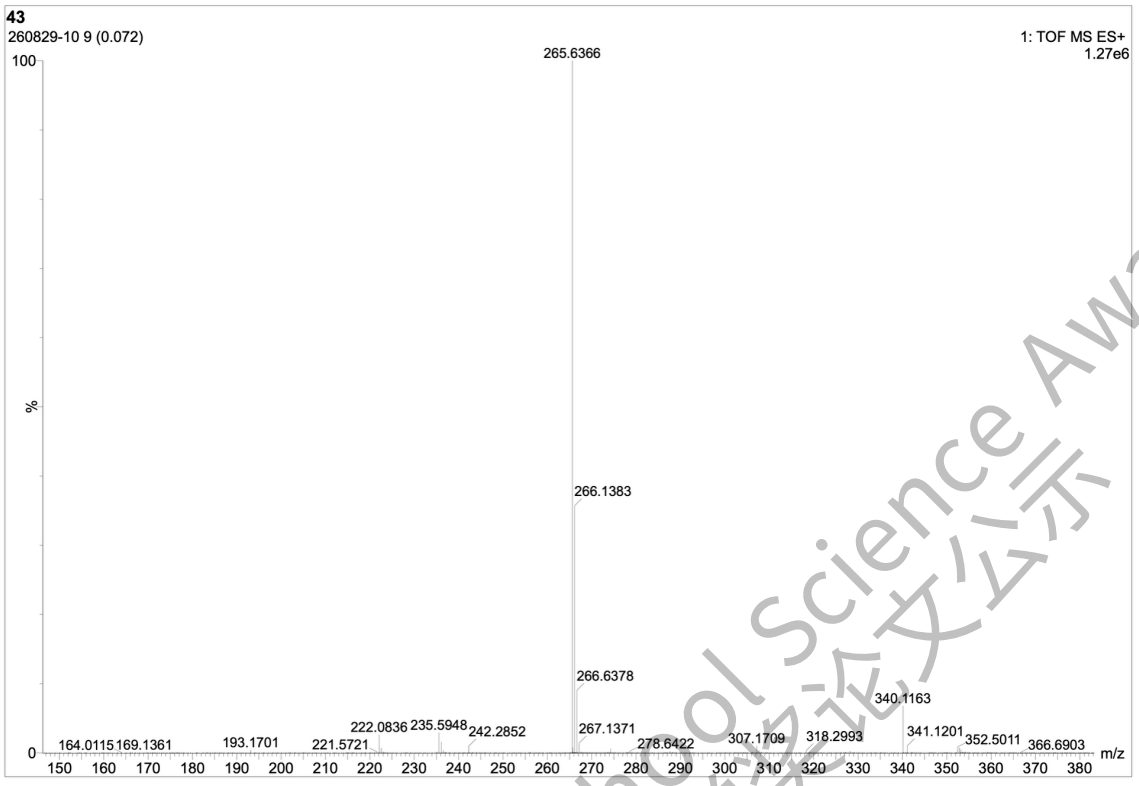


Fig. 16 | High Resolution Mass Spectroscopy of Synthesized TTP-Mem. The tallest m/z peak, 265.6366, confirms the successful synthesis of our product.

3.2 Elucidating the Photophysical Characterization of TTP-Mem

3.2.1 Gaussian Theoretical Calculations

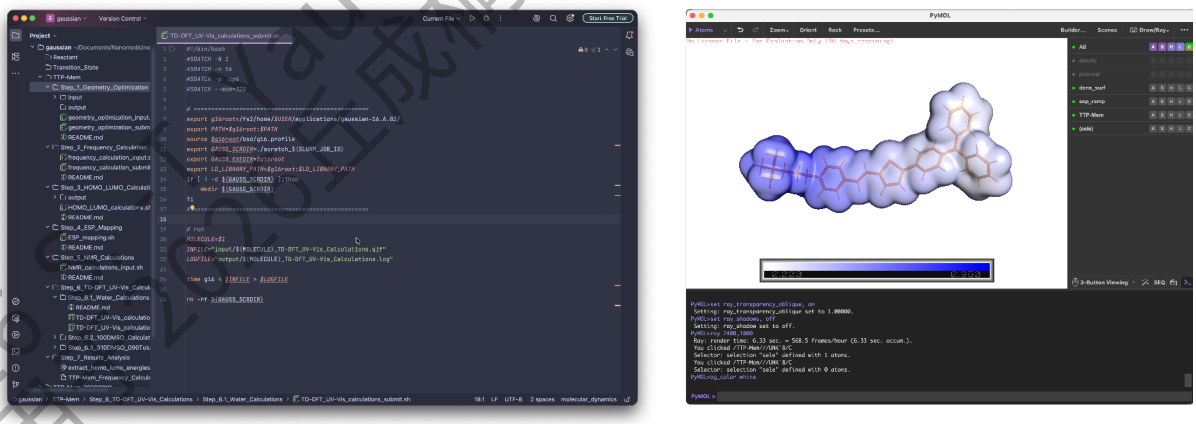


Fig. 17 | Gaussian theoretical calculations preparation and post-run analysis. Screenshot of the PyCharm IDE used to write the input scripts (left). Screenshot of the used PyMol for visualization (right).

Input files for Gaussian theoretical calculations were prepared locally through a pipeline written in `Bash` and guided by `README.md` files for each step; actual Gaussian theoretical calculations were run on a high-performance computing (HPC) cluster. The `m062x` exchange correlation functional (also known as method)

2026 Yau High School Science Award 仅用于2026年成相中学科学论文公示

was chosen over the b3lyp method as m062x more accurately captures the conformational energies of the molecule and reliably predicts the correct lowest-energy conformers [60]. 6-311+G(d,p) was chosen as the basic set. In the 6-311+G(d,p) basic set, the core atomic orbitals are made from a combination of 6 primitive gaussian functions; the valence orbitals are split into three distinct tiers described by a combination of 3, 1, and 1 primitive Gaussian functions (triple-ζ split); diffuse functions (+) adds large orbitals to heavy atoms to capture loose, spreading electron density that are crucial for excited-state calculations and conjugated systems; and polarization functions ((d, p)) adds d-orbitals to heavy atoms and p-orbitals to hydrogens, allowing the electron cloud to distort which enhance accuracy by reproducing bond lengths [61].

Initially, the SMILES encoding of the TTP-Mem molecule was extracted and converted to a Gaussian input file (.gjf) via Open Babel (OBabel). This initial Gaussian input file was then modified using a Bash script to prepare it for geometry optimization. Specifically, the keywords opt=tight int=grid=ultrafine SCRF=(SMD,Solvent=Water) were used. Next, frequency calculations were ran using the optimized geometry with the keywords freq int=grid=ultrafine geom=allcheck guess=read SCRF=(SMD,Solvent=Water). All frequencies were confirmed to be positive, indicating a true minimum energy conformer. From this, the Kohn-Sham-eigenvalues-derived HOMO-LUMO energies and electrostatic potential (ESP) maps were derived using the .chk file and the log file. HOMO-LUMO energies were visualized using VESTA and ESP mapping with PyMOL (unofficial community version). Finally, TD-DFT calculations were ran via Gaussian using the ground-state optimized geometry with the keywords m062x/6-311+g(d,p) #p TD=(NStates=20,Singlets) SCRF=(SMD,Solvent=Water) Geom=AllCheck Guess=Read. The $S_0 \rightarrow S_1$ transition energy, oscillator strength, and electronic transition configuration coefficients were extracted from the output log file.

3.2.2 UV-Vis Absorption and Photoluminescence Spectroscopy

The UV-vis absorption spectrum of TTP-Mem (100 μM) in different pure DMSO, 90% toluene in DMSO (v/v), and 99% PBS in DMSO (v/v) was recorded in the range of 400-700 nm at a scanning rate of 1200 nm/min using a UV-2600i (Shimadzu Corporation, Japan). Spectra were normalized to maximum absorbance and corresponding maximum absorbance wavelengths were recorded.

Fluorescence emission spectra of TTP-Mem (100 μM) in escalating concentrations of toluene in DMSO (0% to 90%, v/v) were acquired using a FL970 fluorescence spectrometer (Techcomp, Tianmei). The sample was excited at 480 nm, excitation and emission slit widths were set to 5 nm, and PMT was set to 600. Emission signals were collected across 500-850 nm. Relative emission intensities (I/I_0) were calculated using:

$$\left(\frac{I}{I_0}\right)_i = \frac{I_{\max,i}}{I_{\max,\,\mathrm{DMSO}}}$$

where $I_{max,i}$ represents the maximum emission intensity at a given solvent composition (i), and $I_{max,DMSO}$ is the maximum emission intensity of TTP-Mem in pure DMSO.

2026 S-I Yau High School Science Award
仅用于2026日成绩中学科学奖公示

3.3 ROS Generation

3.3.1 Ultrasound Irradiation Setup



Fig. 18 | Ultrasound-irradiation setup. Photograph of the ultrasound-irradiation setup used (left). Photograph of the applied ultrasound coupling agent (right-top). Photograph of the irradiation in-progress, with a culture dish placed on top of the transducer (right-bottom).

Ultrasound irradiation was conducted with WED-30, an ultrasonic therapy machine. A thin, uniform layer of ultrasound coupling agent (ultrasound gel) was applied according to the "thin layer" rule to eliminate air pockets between the transducer and the culture dish (Corning 430165, 35mm × 10mm, polystyrene). Ultrasound frequency was set uniformly to 1.0MHz and strength to 1.5w/cm^2 at 50% duty cycle.

3.3.2 Electron Paramagnetic Resonance Spectroscopy

Four groups of samples were prepared for the EPR spectroscopy: two TTP-Mem (5 μM) in DMSO samples and two pure DMSO samples. Each sample was prepared following a standardized protocol with measurements taken at two timepoints (0 min and 5 min post-sonification) to monitor radical generation kinetics.

Singlet Oxygen Detection: To detect singlet oxygen ($^1O_2$), 0.5 mL of the TTP-Mem sample (10 μM) was sonicated, and 100 μL aliquots were withdrawn at 0 and 5 min timepoints. Each aliquot was mixed with 100 μL of 10 mg/L TEMP (2,2,6,6-tetramethylpiperidine) aqueous solution as the spin-trapping agent. The resulting mixture was transferred into a quartz NMR capillary tube for EPR measurement (final TTP-Mem concentration: 5 μM).

Superoxide Anion Detection: To detect superoxide anion ($O_2^{\bullet-}$), 0.5 mL of the TTP-Mem sample (10 μM) was sonicated, and 100 μL aliquots were withdrawn at 0 and 5 min timepoints. Each aliquot was mixed with 100 μL of 10 mg/L TEMP (2,2,6,6-tetramethylpiperidine) in methanol as the spin-trapping agent. The

2026 S. T. Yau High School Science Award
仅用于2026丘成桐中学科学奖论文评审

resulting mixture was transferred into a quartz NMR capillary tube for EPR measurement (final TTP-Mem concentration: 5 μM).

Hydroxyl Radical Detection: To detect hydroxyl radicals (•OH), 0.5 mL of the TTP-Mem sample (10 μM) was sonicated, and 100 μL aliquots were withdrawn at 0 and 5 min timepoints. Each aliquot was mixed with 100 μL of 10 mg/L DMPO (5,5-dimethyl-1-pyrroline N-oxide) aqueous solution (in water) as the spin-trapping agent. The resulting mixture was transferred into a quartz NMR capillary tube for EPR measurement (final TTP-Mem concentration: 5 μM).

Ultrasound irradiation was conducted under 1.5w/cm^2 for 5 minutes under 1.0MHz, 50% duty cycle. EPR was measured with Bruker A300 with microwave frequency set to 9.854854 GHz. Double integral signals were calculated using the built-in analysis function of GraphPad Prism 10.

3.3.3 Time-Course ABDA Absorbance Spectroscopy

The absorbance spectra of TTP-Mem (5 μM) and the ABDA Absorbance-Based probe (10 μM) under different ultrasound irradiation times was recorded in the range of 300-450 nm at a scanning rate of 1200 nm/min using a UV-2600i (Shimadzu Corporation, Japan). Relative absorption intensities (I/I_0) were calculated using:

$$\left(\frac{I}{I_0}\right)_t = \frac{I_{\max,t}}{I_{\max,\,0\ \min}}$$

where $I_{\max,t}$ represents the maximum absorption intensity at λ= 400 nm under ultrasound irradiation for t minutes, and $I_{\max,0\ \min}$ is the maximum absorption intensity of TTP-Mem without ultrasound irradiation.

3.4 GROMACS Molecular Dynamics Simulations

GROMACS molecular dynamics (MD) simulations were used to verify membrane-anchoring capabilities. Each step of the GROMACS MD simulations is well-documented in `README.md` file. All MD simulations were ran designed locally and ran on the HPC cluster.

Step 3.4.1: Building the Membrane

Calculated Number of Lipids:

Lipid Type	Upperleaflet Number	Lowerleaflet Number
Cholesterol	55	55
POPC	55	55
POPE	55	55
POPS	55	55

Calculated XY System Size:

	Upperleaflet	Lowerleaflet
Protein Area	0	0
Lipid Area	12512.5	12512.5
# of Lipids	220	220
Total Area	12512.5	12512.5
Average Area	12512.50	
A	120.20	
B	120.20	

2026 S.-T. Yau High School Science Award
仅用于2026丘成桐中学科学奖论文公示

Fig. 19 | CHARMM-GUI ratio inputs. Screenshot of the CHARMM-GUI lipid ratio inputs and calculated average area. A symmetrical leaflet and hexagonal simulation box were employed.

The membrane was built using CHARMM-GUI: Membrane Builder tool [62], [63]. A 1:1:1:1 ratio of POPC (1-palmitoyl-2-oleoyl-glycero-3-phosphocholine), POPE (1-palmitoyl-2-oleoyl-glycero-3-phosphoethanolamine), POPS (1-palmitoyl-2-oleoyl-glycero-3-phosphoserine), and CHL1 (Cholesterol) was used. A hexagonal simulation box was utilized (`SET A = 120.200626`, `SET B = 120.200626`, `SET C = 220`, `SET GAMMA = 120.0`), with water height set to 202.5 angstroms to provide ample space for steered molecular dynamics simulation (SMD). The CHARMM-36 forcefield was selected and sodium chloride (NaCl) as the solvent.

Step 3.4.2: Parameterizing the Ligand

`Obabel` was utilized to convert the `SMILES` encoded TTP-Mem molecule to `.mol2` format. This input was then parameterized via CHARMM General Forcefield (`CGenFF`) [64] and converted to a `GROMACS`-compatible format via a conversion script (`charmm2gmx`) found on GitHub.

Step 3.4.3: Membrane Equilibration

The pure membrane system was equilibrated using the CHARMM-GUI generated setup, consisting of an energy-minimization stage converging at 4290 steps (maximum force for convergence: 1000.0 kJ/mol/nm; maximum steps: 5000, LINCS constraints), several NVT ensembles that slowly converge to the predetermined 310.15 K and several NPT ensembles that maintain 310.15K and converges to 1 bar under loosening lipid restraints (position restraints: `DPOSRES_FC_LIPID`; dihedral restraints: `DDIHRES_FC`).

Step 3.4.4: Lipid Insertion

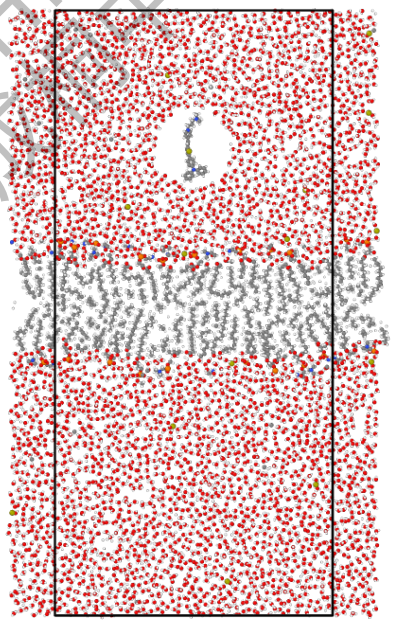


Fig. 20 | Successful insertion of the ligand into the solvent system. OVITO rendered image of the ligand inserted in the cleared cavity.

2026 S.-T. Yau High School Science Award
仅用于2026丘成桐中学科学奖公示

The TTP-Mem ligand was inserted into the aqueous phase 6 nm above the bilayer midplane. A cavity in the solvent at the insertion site was generated prior to insertion to avoid unfavorable ligand-solvent overlap using `MDAnalysis` (which was also used to align the ligand along the z-axis), and the ligand was placed with `gmx insert-molecules`. The system was subsequently neutralized with NaCl, yielding a final system of 261,838 atoms.

Step 3.4.5: Membrane-Ligand System Equilibration

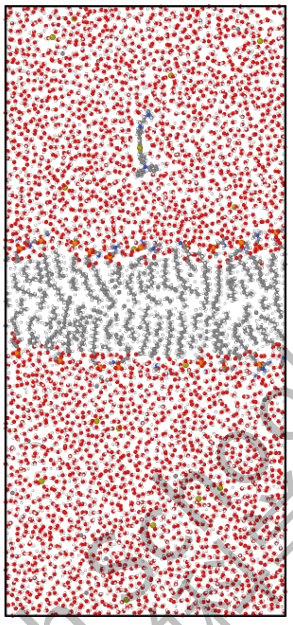


Fig. 21 | Successful equilibration of the ligand-membrane system. OVITO rendering of the ligand after successful insertion into the solvent, surrounded by liquid particles, indicative of system equilibration.

The ligand was positionally restrained (k = 1000 kJ mol^{-1} nm^{-2}) during steepest-descent energy minimization (converged to a maximum force below 1000 kJ mol^{-1} nm^{-2}) followed by 100 ps of NVT and 100 ps of NPT dynamics. Restraints were then loosened (k = 100 kJ mol^{-1} nm^{-2}) for a further 500 ps of NPT equilibration at the bulk-water position, allowing the ligand's hydration shell and nearby ions to relax, providing a good starting position.

Step 3.4.6: Steered Molecular Dynamics (SMD)

The ligand was pulled into the upper leaflet over 2.5 ns using a two-coordinate pulling protocol. A harmonic umbrella potential (k = 1000 kJ mol^{-1} nm^{-2}) was applied to the projection of the membrane–ligand center-of-mass separation onto the bilayer normal, with the reference moving at a constant rate of 2 nm ns^{-1} from the equilibrated separation (5.61 nm) to a final depth of ~0.6 nm. In parallel, an orientation umbrella (k = 200 kJ mol rad^{-2}) restrained the angle between the ligand head-to-tail vector and the membrane normal to 20°, matching the mean lipid tilt of the membrane and enforcing a head-first, upright insertion pathway. (An initial one-coordinate protocol lacking the orientation restraint permitted thermal rotation of the ligand and amine-first insertion; the two-coordinate design was adopted to enforce the intended pathway.) The pulled configuration was then equilibrated for 10 ns at the final SMD position, and finally simulated freely

2026 S.-T. Yau High School Science Award
仅用于2026丘成桐中学科学奖论文公示

(unrestrained) for 10 ns with the pulling potentials set to zero to passively monitor ligand-membrane separation and ligand orientation to confirm drug design and to identify the preferred binding pocket.

Step 3.4.7: Umbrella Sampling and Potential of Mean Force Analysis

The binding free-energy profile was computed on SMD-extracted membrane-ligand separation windows via umbrella sampling. A total of 20 independent windows spanning 0.9-3.9 nm were initiated from first-passage frames extracted along the steered trajectory, with spring constants of 1000 kJ mol^{-1} nm^{-2} in the binding pocket (0.9-1.6 nm, 0.1 nm spacing) and 500 kJ mol^{-1} nm^{-2} along the desorption pathway (1.75-3.9 nm, 0.25-0.3 nm spacing), giving force-constant widths ($\sigma \approx 0.05$ and 0.07 nm, respectively) consistent with the window spacing. Three additional midpoint windows (2.125, 2.875, 3.45 nm) were included to guarantee adjacent-window overlap. Windows were run for 1.5 ns (pocket, 2.25 ns) with the initial 0.5 ns (pocket, 0.75 ns) discarded as equilibration, and the ligand orientation was left unrestrained but monitored throughout. Potentials of mean force were reconstructed with the weighted histogram analysis method [65] using 100 bootstrap samples for uncertainty estimation. Finally, the PMF is reported over the binding-pocket region (0.9–2.25 nm), covered by 11 windows with continuously overlapping histograms.

3.5 Human Foreskin Fibroblast (HFF) Cells and *T. gondii* Culturing

Human Foreskin Fibroblast (HFF) cells were used as host cells for the routine culture and propagation of *Toxoplasma gondii* RH tachyzoites. HFF cells were maintained in **D**ulbecco's **m**odified **E**agle **m**edium (DMEM), supplemented with 10% **f**etal **b**ovine **s**erum (FBS) and 1% penicillin-streptomycin (abbreviated as D10) at 37 °C in a humified 5% CO_2 incubator. HFF cells were passaged at 80%-90% confluence using 0.25% trypsin-EDTA followed by centrifugation at 1,000 × *g* for 3 min. *T. gondii* tachyzoites were routinely maintained via serially passage in HFF monolayers after detachment by cell scraping, syringe aspiration for host cell disruption, and purification through a 5 μm pore-size filter, and centrifugation at 1,000 × *g* for 10 min. Importantly, *T. gondii* RH tachyzoites were maintained using DMEM supplemented with 2% FBS and 1% penicillin-streptomycin (abbreviated here as D2), different to the 10% used in HFF cells culturing.

3.6 Organelle Colocalization

To experimentally verify the membrane affinity of TTP-Mem, freshly isolated RH strain tachyzoites were resuspended in phosphate buffered solution after release by cell scraping, syringe aspiration, purification, and centrifugation at 1,000 × *g* for 10 min. Here, PBS was used to ensure that DMEM would not interfere with TTP-Mem was added to both groups (5 μM), DiIC12 to the experimental group (5 μM) and ER Tracker to the negative control group (10 μM). The samples were incubated for 30 min at 37 °C in a humidified 5% CO_2 incubator. The colocalization images were then obtained from confocal laser scanning microscopy (CLSM; Leica). TTP-Mem fluorescence was collected at λex = 488 nm, λem = 650-750 nm; DiIC12 and ER-Tracker fluorescence signals were both collected at λex = 561 nm, λem = 560-650 nm. Fluorescent intensities were then extracted from Fiji (open-source image processing package based on ImageJ2) via the `Image > Adjust > Color Threshold` tool and the `Analyze > Plot Profile` tool. Pearson correlation coefficients were calculated using the built-in analysis function of GraphPad Prism10.

2026 S.T. Yau High School Science Award
仅用于2026丘成桐中学科学奖论文公示

3.7 Evaluation of Parasite Viability and Membrane Integrity Following SDT

3.7.1 Calcein/PI (Live/Dead) Staining for T. gondii

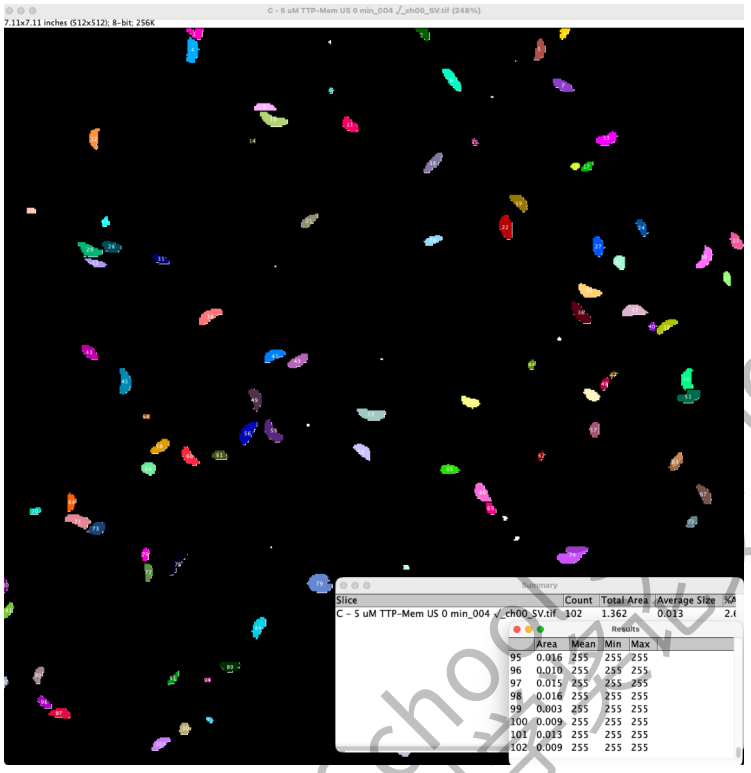


Fig. 22 | Fiji cell-counting setup. Screenshot of the self-developed cell-counting setup in use.

Freshly isolated RH strain tachyzoites were resuspended in D2 after release by cell scraping, syringe aspiration, purification, and centrifugation at 1,000 × *g* for 10 min. This solution was then divided between different 10mm × 35 mm petri dishes and TTP-Mem (5 µM) was subsequently added. The samples were incubated for 10 min at 37 °C in a humidified 5% CO_2 incubator, followed by ultrasound irradiation at 1.5w/cm^2, 1.0MHz for 3 min using the setup shown in Section 3.3.1. Subsequently, the samples were centrifuged at 1,000 × *g* for 12 min, this extended duration chosen to ensure complete pelleting of non-viable parasites alongside intact ones. The samples were then suspended in the Calcein AM/PI assay buffer (with Calcein AM and PI diluted 1:1000 in assay buffer) from Beyotime Biotechnology. Finally, the samples were incubated for 30 min at 37 °C in a humidified 5% CO_2 incubator, then observed via CLSM (Leica). TTP-Mem fluorescence was collected at λex = 488 nm, λem = 650-750 nm; Calcein at λex = 488 nm, λem = 500-540 nm; and PI at λex = 561 nm, λem = 590-640 nm. 6 positions for each sample were collected and cell counting was conducted in Fiji through a self-developed ImageJ plugin (download and documentation available on GitHub here). The obtained Calcein/PI cell counts were analyzed with one-way Welch's ANOVA and Games-Howell post-hoc test through `Python` (available on Google Colab here). The Games-Howell post-hoc test was chosen because no equal variance between the groups can be assumed.

3.7.2 Detection of Membrane-Proximal ROS via Singlet Oxygen Sensor Green

Freshly isolated RH strain tachyzoites were resuspended in D2 after release by cell scraping, syringe aspiration, purification, and centrifugation at 1,000 × *g* for 10 min. This solution was then divided between

2026 Science Award 仅用于2026日本科学奖公示 Yau High School

different 10mm × 35 mm petri dishes and TTP-Mem (5 μM), singlet oxygen sensor green (SOSG; 10 μM, Beyotime), and Hoechst 33258 (diluted 1:500, CAS 23491-45-4, Beyotime) were then added and samples were incubated for 20 min at 37 °C in a humidified 5% CO_2 incubator. SDT procedures as described for the Calcein/PI assay were performed here. After centrifugation, the samples were then resuspended in 100 μL PBS, then observed via CLSM (Leica). TTP-Mem fluorescence was collected at λex = 488 nm, λem = 650-750 nm; SOSG at λex = 488 nm, λem = 500-550 nm; and Hoechst at λex = 405 nm, λem = 410-480 nm.

3.7.3 Morphological Evaluation by Scanning Electron Microscopy

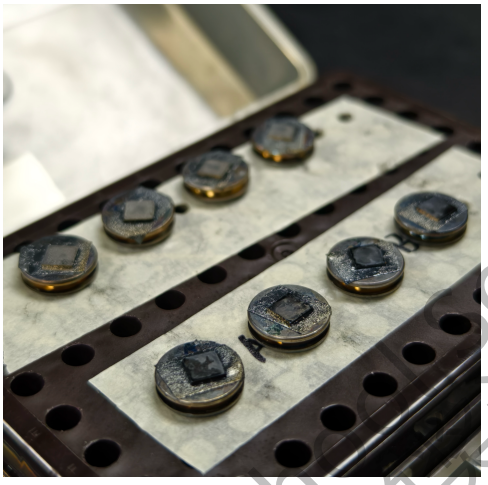


Fig. 23 | Preparation of scanning electron microscopy samples. Photograph of the prepared SEM samples drop casted and dried on the silicon wafer.

Scanning electron microscopy (SEM) was utilized to evaluate the morphological damage to tachyzoites following TTP-Mem-mediated SDT. Parasite isolation and subsequent SDT were performed as described above (Section 3.7.2), with a pre-incubation period of 10 min with TTP-Mem (5 μM) at 37 °C in a humidified 5% CO_2 incubator prior to ultrasound irradiation. Centrifugation was performed at 1,000 × *g* for 12 min. Again, the increased centrifugation time was chosen to ensure complete pelleting of non-viable parasites alongside intact ones. Tachyzoites were then fixed in glutaraldehyde (500 μL per sample) at 4 °C overnight), followed by centrifugation at 1,000 × *g* for 12 min to remove the fixative. The sample was then drop casted onto a silicon wafer and allowed to air-dry. Dehydration was performed via a graded series of ethanol/ddH_2O (30%→40%→50%→60%→70%→80%→90%→100%→100%, v/v), with each step allowed to air-dry. The sample was then sputter-coated with gold (power = 10 W, time = 300 s, pressure = 8 Pa) and imaged using a scanning electron microscope (Phenom Pharos G2, Thermo Fisher Scientific) at an accelerating voltage of 15 kV using a secondary electron detector probe (SED).

3.5 In Vitro Plaque Assay for Parasite Viability and Proliferation Assessment

Two crystal violet plaque assay was used to evaluate TTP-Mem SDT antiparasitic efficacy. Freshly isolated *T. gondii* were extracted using the protocol described in Section 3.7.2. TTP-Mem was then added at varying concentrations (0 μM, 5 μM, 15 μM, and 45 μM) and incubated at 37 °C in a humidified 5% CO_2 incubator for 10 minutes. Ultrasound irradiation was applied for a reduced duration of 1.5 min (compared to the 3.0 min utilized in Section 3.7.2) to prevent excessive, complete parasite eradication, thereby enabling the

2026 Siyau High School Science Award
仅用于2026年成柳中学科学奖论文公示

observation of drug concentration-dependent sonodynamic effects. Following SDT, centrifugation was then performed at 1,000 × *g* for 11 min to remove the drug, followed by resuspension in 200 µL D2. A 10 µL aliquot of the suspension from the untreated group (no TTP-Mem and no US) was loaded onto a hemocytometer for parasite counting under an optical microscope. Based on this count, the volume corresponding to 1000 control tachyzoites was calculated, and an equivalent volume was inoculated from each group onto the confluent HFF monolayers cultured in 12-well plates. The plates were incubated undisturbed at 37 °C for 7 days. The monolayers were then fixed with 4% paraformalydehyde (PFA) for 10 min then stained with 0.1% crystal violet for 30 min at room temperature. Finally, gentle washing was used to remove detached debris, followed by drying at 60 °C in a laboratory oven.

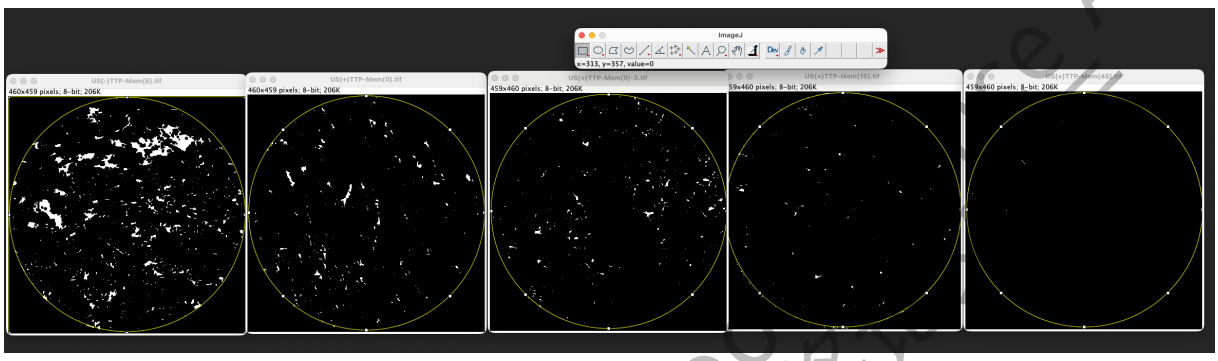


Fig. 24 | ImageJ plaque area calculations. Screenshot of the self-developed pipeline in ImageJ used to calculate plaque areas. The yellow ring around the plate represents the selected ROI.

Lytic plaque areas were analyzed in ImageJ through a self-developed pipeline. First, the image was converted to a `16-bit`. A `threshold` and the `erode` function were uniformly applied across all pictures. Here, the `erode` function is critical to eliminate the "mosaic-style" plaque that is naturally occurring between HFF cells, without which ImageJ would falsely identify as plaque. Finally, a region of interest (ROI) was applied and plaque area was measured.

4. Conclusion

This study presents the first novel use of SDT in the treatment of *T. gondii* to overcome the limitations of current clinical treatments. We first synthesized the AIE sonosensitizer, TTP-Mem, from commercially available material through a two-step reaction, and analyzed the key reaction mechanisms. We then performed theoretical calculations in Gaussian and experimentally characterized photophysical properties of TTP-Mem, revealing AIE behavior under increasing toluene concentrations, with a fluorescent intensity increase of nearly 30-fold. To analyze the ROS generation efficiency of TTP-Mem under ultrasound-irradiation, we utilized EPR spectra and time-course ABDA absorbance assays, revealing a 100-fold boost in the production of Type II (singlet oxygen) ROS that complements the predominant Type I ROS that forms under ultrasound alone. TTP-Mem membrane-anchoring functionalities were simulated via GROMACS MD simulations and experimentally verified through organelle colocalization analysis, obtaining a high correlation-coefficient of 0.78. Calcein/PI (live/dead) staining reveals an antiparasitic efficacy of 80.4% under just 3 min of ultrasound irradiation when compared to the control group (no ultrasound activation), with the SOSG probe confirming in vitro Type II ROS generation as potential mechanism behind *T. gondii*

2026 S.T. Yau High School Science Award
仅用于2026丘成桐中学生科学奖

inactivation via TTP-Mem SDT. We next employed SEM to visualize membrane rupture as the root-cause of *T. gondii* death under TTP-Mem SDT. Finally, crystal violet plaque assays establish TTP-Mem SDT functional therapeutic efficacy as dependent of TTP-Mem concentrations, with 84.3%, 96.3%, and 99.86% plaque reduction rate at 5 μM, 15 μM, and 45 μM of TTP-Mem under just 90 seconds of ultrasound irradiation, respectively. Taken together, this study successfully demonstrates the feasibility and efficacy of TTP-Mem SDT as a promising strategy for the inactivation of *T. gondii* cells, circumventing major clinical limitations of current therapies, including delayed onset and drug-resistance. Beyond parasitology, these findings provide robust experimental support for the potential application of SDT in treatment of deep-seated parasitic infections, granting meaningful insights into critical public health challenges associated with pervasive parasitic diseases.

Data availability statement

All data generated or analyzed in this paper are available from the corresponding author upon reasonable request.

References

[1] J. Luo *et al.*, "Aggregation-induced emission of 1-methyl-1,2,3,4,5-pentaphenylsilole," *Chem. Commun.*, no. 18, pp. 1740–1741, 2001, doi: 10.1039/b105159h.

[2] G. Jiang, J. Liu, and P. Zhou, "Unraveling the Mechanism of ACQ-to-AIE Transformation of Fluorescein Derivatives," *J. Phys. Chem. A*, vol. 127, no. 24, pp. 5193–5201, Jun. 2023, doi: 10.1021/acs.jpca.3c02244.

[3] C. Ji, L. Lai, P. Li, Z. Wu, W. Cheng, and M. Yin, "Organic dye assemblies with aggregation-induced photophysical changes and their bio-applications," *Aggregate*, vol. 2, no. 4, p. e39, 2021, doi: 10.1002/agt2.39.

[4] J. Zhang, H. Zhang, J. W. Y. Lam, and B. Z. Tang, "Restriction of Intramolecular Motion(RIM): Investigating AIE Mechanism from Experimental and Theoretical Studies," *Chem. Res. Chin. Univ.*, vol. 37, no. 1, pp. 1–15, Feb. 2021, doi: 10.1007/s40242-021-0381-6.

[5] N. L. C. Leung *et al.*, "Restriction of Intramolecular Motions: The General Mechanism behind Aggregation-Induced Emission," *Chem. – Eur. J.*, vol. 20, no. 47, pp. 15349–15353, 2014, doi: 10.1002/chem.201403811.

[6] X. Lim, "The nanolight revolution is coming," *Nature*, vol. 531, no. 7592, pp. 26–28, Mar. 2016, doi: 10.1038/531026a.

[7] Z. Wu *et al.*, "Construction of Heterogeneous Aggregation-Induced Emission Microspheres with Enhanced Multi-Mode Information Encryption," *Molecules*, vol. 29, no. 24, p. 5852, Dec. 2024, doi: 10.3390/molecules29245852.

[8] Q. Wei, J. Zhang, and Z. Ge, "AIE-active Emitters and Their Applications in OLEDs", Accessed: Sep. 13, 2026. [Online]. Available: https://onlinelibrary.wiley.com/doi/10.1002/9781119643098.ch41

[9] H. Wang *et al.*, "Aggregation-Induced Emission (AIE), Life and Health," *ACS Nano*, vol. 17, no. 15, pp. 14347–14405, Jul. 2023, doi: 10.1021/acsnano.3c03925.

[10] D. Yadav, V. D. Singh, A. Kumar, S. Kumar, and R. S. Singh, "High-Resolution Latent Fingerprinting by AIE-Active Light-Harvesting BODIHYs and pH-Induced Configurational Molecular Switching in Hydrazones," *ACS Appl. Opt. Mater.*, vol. 4, no. 6, pp. 1707–1718, May 2026, doi: 10.1021/acsaom.6c00117.

[11] Z. Sheng *et al.*, "Bright Aggregation-Induced-Emission Dots for Targeted Synergetic NIR-II Fluorescence and NIR-I Photoacoustic Imaging of Orthotopic Brain Tumors," *Adv. Mater.*, vol. 30, no. 29, p. 1800766, 2018, doi: 10.1002/adma.201800766.

[12] H. Yu *et al.*, "AIE-Active Photosensitizers: Manipulation of Reactive Oxygen Species Generation and Applications in Photodynamic Therapy," *Biosensors*, vol. 12, no. 5, p. 348, May 2022, doi: 10.3390/bios12050348.

2026 Shanghai School Science Award 仅用于2026上海科学奖论文公示

[13] Z. Zhang *et al.*, "Aggregation-induced emission biomaterials for anti-pathogen medical applications: detecting, imaging and killing," *Regen. Biomater.*, vol. 10, p. rbad044, Jan. 2023, doi: 10.1093/rb/rbad044.
[14] T. Sun, J. Song, W. Zhang, L. Tan, J. Dong, and Y. Li, "A review of AIE-based theranostic strategies regarding antibiotic-tolerant microbial infections," *Chem. Commun.*, vol. 61, no. 91, pp. 17751–17769, Nov. 2025, doi: 10.1039/d5cc04510j.
[15] C. Zhu, R. T. K. Kwok, J. W. Y. Lam, and B. Z. Tang, "Aggregation-Induced Emission: A Trailblazing Journey to the Field of Biomedicine," *ACS Appl. Bio Mater.*, vol. 1, no. 6, pp. 1768–1786, Oct. 2018, doi: 10.1021/acsabm.8b00600.
[16] A. J. P. O. de Almeida *et al.*, "ROS: Basic Concepts, Sources, Cellular Signaling, and its Implications in Aging Pathways," *Oxid. Med. Cell. Longev.*, vol. 2022, p. 1225578, Oct. 2022, doi: 10.1155/2022/1225578.
[17] H. J. Shields, A. Traa, and J. M. Van Raamsdonk, "Beneficial and Detrimental Effects of Reactive Oxygen Species on Lifespan: A Comprehensive Review of Comparative and Experimental Studies," *Front. Cell Dev. Biol.*, vol. 9, p. 628157, Feb. 2021, doi: 10.3389/fcell.2021.628157.
[18] Y. Li *et al.*, "A Bifunctional Aggregation-Induced Emission Luminogen for Monitoring and Killing of Multidrug-Resistant Bacteria," *Adv. Funct. Mater.*, vol. 28, no. 42, p. 1804632, 2018, doi: 10.1002/adfm.201804632.
[19] D. Hill and J. P. Dubey, "Toxoplasma gondii: transmission, diagnosis and prevention," *Clin. Microbiol. Infect.*, vol. 8, no. 10, pp. 634–640, Oct. 2002, doi: 10.1046/j.1469-0691.2002.00485.x.
[20] J. G. Montoya and O. Liesenfeld, "Toxoplasmosis," *The Lancet*, vol. 363, no. 9425, pp. 1965–1976, Jun. 2004, doi: 10.1016/S0140-6736(04)16412-X.
[21] G. Pappas, N. Roussos, and M. E. Falagas, "Toxoplasmosis snapshots: Global status of *Toxoplasma gondii* seroprevalence and implications for pregnancy and congenital toxoplasmosis," *Int. J. Parasitol.*, vol. 39, no. 12, pp. 1385–1394, Oct. 2009, doi: 10.1016/j.ijpara.2009.04.003.
[22] H. G. Ehmen and C. G. K. Lüder, "Long-Term Impact of Toxoplasma gondii Infection on Human Monocytes," *Front. Cell. Infect. Microbiol.*, vol. 9, p. 235, Jun. 2019, doi: 10.3389/fcimb.2019.00235.
[23] C. J. Ramírez-Flores and R. Mondragón-Flores, "Comprehensive analysis of Toxoplasma gondii migration routes and tissue dissemination in the host," *PLoS Negl. Trop. Dis.*, vol. 19, no. 7, p. e0013369, Jul. 2025, doi: 10.1371/journal.pntd.0013369.
[24] S. Liu *et al.*, "Comprehensive Insights into the Development of Antitoxoplasmosis Drugs: Current Advances, Obstacles, and Future Perspectives," *J. Med. Chem.*, vol. 67, no. 23, pp. 20740–20764, Nov. 2024, doi: 10.1021/acs.jmedchem.4c01733.
[25] A. L. Sutterland *et al.*, "Beyond the association. *Toxoplasma gondii* in schizophrenia, bipolar disorder, and addiction: systematic review and meta-analysis," *Acta Psychiatr. Scand.*, vol. 132, no. 3, pp. 161–179, Sep. 2015, doi: 10.1111/acps.12423.
[26] D. G. Contopoulos-Ioannidis, M. Gianniki, A. Ai-Nhi Truong, and J. G. Montoya, "Toxoplasmosis and Schizophrenia: A Systematic Review and Meta-Analysis of Prevalence and Associations and Future Directions," *Psychiatr. Res. Clin. Pract.*, vol. 4, no. 2, pp. 48–60, Jun. 2022, doi: 10.1176/appi.prcp.20210041.
[27] E. F. Torrey and R. H. Yolken, "*Toxoplasma gondii* and Schizophrenia," *Emerg. Infect. Dis.*, vol. 9, no. 11, pp. 1375–1380, Nov. 2003, doi: 10.3201/eid0911.030143.
[28] S. Vlatkovic *et al.*, "Increased prevalence of Toxoplasma gondii seropositivity in patients with treatment-resistant schizophrenia," *Schizophr. Res.*, vol. 193, pp. 480–481, Mar. 2018, doi: 10.1016/j.schres.2017.08.006.
[29] O. Djurković-Djaković, J. Dupouy-Camet, J. Van der Giessen, and J. P. Dubey, "Toxoplasmosis: Overview from a One Health perspective," *Food Waterborne Parasitol.*, vol. 15, p. e00054, Apr. 2019, doi: 10.1016/j.fawpar.2019.e00054.
[30] J. M. Brooks, G. L. Carrillo, J. Su, D. S. Lindsay, M. A. Fox, and I. J. Blader, "Toxoplasma gondii Infections Alter GABAergic Synapses and Signaling in the Central Nervous System," *mBio*, vol. 6, no. 6, p. 10.1128/mbio.01428-15, Oct. 2015, doi: 10.1128/mbio.01428-15.
[31] B. J. Luft and J. S. Remington, "Toxoplasmic Encephalitis in AIDS," *Clin. Infect. Dis.*, vol. 15, no. 2, pp. 211–222, Aug. 1992, doi: 10.1093/clinids/15.2.211.
[32] B. L. Castaño *et al.*, "Sulfadiazine Plus Pyrimethamine Therapy Reversed Multiple Behavioral and Neurocognitive Changes in Long-Term Chronic Toxoplasmosis by Reducing Brain Cyst Load and Inflammation-Related Alterations," *Front. Immunol.*, vol. 13, p. 822567, Apr. 2022, doi: 10.3389/fimmu.2022.822567.

2026 Shanghai High School Science Award 仅用于2026上海市高中学科竞赛公示

[33] J. B. Rodriguez and S. H. Szajnman, "An updated review of chemical compounds with anti-Toxoplasma gondii activity," *Eur. J. Med. Chem.*, vol. 262, p. 115885, Dec. 2023, doi: 10.1016/j.ejmech.2023.115885.
[34] N. Konstantinovic, H. Guegan, T. Stäjner, S. Belaz, and F. Robert-Gangneux, "Treatment of toxoplasmosis: Current options and future perspectives," *Food Waterborne Parasitol.*, vol. 15, p. e00036, Apr. 2019, doi: 10.1016/j.fawpar.2019.e00036.
[35] M. Montazeri *et al.*, "Drug Resistance in Toxoplasma gondii," *Front. Microbiol.*, vol. 9, p. 2587, Oct. 2018, doi: 10.3389/fmicb.2018.02587.
[36] J. Chen *et al.*, "An AIE photosensitizer with type I/II ROS generation for photodynamic therapy of toxoplasmosis," *Chem. Commun.*, vol. 62, no. 7, pp. 2247–2250, Jan. 2026, doi: 10.1039/d5cc04690d.
[37] G. Gunaydin, M. E. Gedik, and S. Ayan, "Photodynamic Therapy—Current Limitations and Novel Approaches," *Front. Chem.*, vol. 9, p. 691697, Jun. 2021, doi: 10.3389/fchem.2021.691697.
[38] L. Fan, A. Idris Muhammad, B. Bilyaminu Ismail, and D. Liu, "Sonodynamic antimicrobial chemotherapy: An emerging alternative strategy for microbial inactivation," *Ultrason. Sonochem.*, vol. 75, p. 105591, Jul. 2021, doi: 10.1016/j.ultsonch.2021.105591.
[39] Y. Xie, J. Hu, W. Lei, and S. Qian, "Prediction of vascular injury by cavitation microbubbles in a focused ultrasound field," *Ultrason. Sonochem.*, vol. 88, p. 106103, Aug. 2022, doi: 10.1016/j.ultsonch.2022.106103.
[40] X. Lin, J. Song, X. Chen, and H. Yang, "Ultrasound-Activated Sensitizers and Applications," *Angew. Chem. Int. Ed.*, vol. 59, no. 34, pp. 14212–14233, 2020, doi: 10.1002/anie.201906823.
[41] L. Rengeng, Z. Qianyu, L. Yuehong, P. Zhongzhong, and L. Libo, "Sonodynamic therapy, a treatment developing from photodynamic therapy," *Photodiagnosis Photodyn. Ther.*, vol. 19, pp. 159–166, Sep. 2017, doi: 10.1016/j.pdpdt.2017.06.003.
[42] B. Liu *et al.*, "The influence of ultrasound on the fluoroquinolones antibacterial activity," *Ultrason. Sonochem.*, vol. 18, no. 5, pp. 1052–1056, Sep. 2011, doi: 10.1016/j.ultsonch.2011.02.001.
[43] J. Yu *et al.*, "Gastric Acid-Responsive ROS Nanogenerators for Effective Treatment of *Helicobacter pylori* Infection without Disrupting Homeostasis of Intestinal Flora", doi: 10.1002/advs.202206957.
[44] H.-Q. Dong, X.-F. Fu, M.-Y. Wang, and J. Zhu, "Research progress on reactive oxygen species production mechanisms in tumor sonodynamic therapy," *World J. Clin. Cases*, vol. 11, no. 22, pp. 5193–5203, Aug. 2023, doi: 10.12998/wjcc.v11.i22.5193.
[45] W. Cai *et al.*, "Efficient antibacterial AIEgens induced ROS for selective photodynamic treatment of bacterial keratitis," *Front. Chem.*, vol. 10, Jan. 2023, doi: 10.3389/fchem.2022.1088935.
[46] M. Y. Berezin and S. Achilefu, "Fluorescence Lifetime Measurements and Biological Imaging," *Chem. Rev.*, vol. 110, no. 5, pp. 2641–2684, May 2010, doi: 10.1021/cr900343z.
[47] "5.12: Electron Paramagnetic Resonance (EPR) of Membranes," Physics LibreTexts. Accessed: Sep. 07, 2026. [Online]. Available: https://phys.libretexts.org/Courses/University_of_California_Davis/Biophysics_241%3A_Membrane_Biology/05%3A_Experimental_Characterization_-_Spectroscopy_and_Microscopy/5.12%3A_Electron_Paramagnetic_Resonance_(EPR)_of_Membranes
[48] "EPR - Theory," Chemistry LibreTexts. Accessed: Sep. 07, 2026. [Online]. Available: https://chem.libretexts.org/Bookshelves/Physical_and_Theoretical_Chemistry_Textbook_Maps/Supplemental_Modules_(Physical_and_Theoretical_Chemistry)/Spectroscopy/Magnetic_Resonance_Spectroscopies/Electron_Paramagnetic_Resonance/EPR_-_Theory
[49] S. Zhang, V. Lloveras, Y. Wu, J. Tolosa, J. C. García-Martínez, and J. Vidal-Gancedo, "Fluorescent and Magnetic Radical Dendrimers as Potential Bimodal Imaging Probes," *Pharmaceutics*, vol. 15, no. 6, p. 1776, Jun. 2023, doi: 10.3390/pharmaceutics15061776.
[50] S. Wierzbicki, J. C. Douglin, A. Kostuch, D. R. Dekel, and K. Kruczała, "Are Radicals Formed During Anion-Exchange Membrane Fuel Cell Operation?," *J. Phys. Chem. Lett.*, vol. 11, no. 18, pp. 7630–7636, Aug. 2020, doi: 10.1021/acs.jpclett.0c02349.
[51] J. Chauvin, F. Judée, M. Yousfi, P. Vicendo, and N. Merbahi, "Analysis of reactive oxygen and nitrogen species generated in three liquid media by low temperature helium plasma jet," *Sci. Rep.*, vol. 7, no. 1, p. 4562, Jul. 2017, doi: 10.1038/s41598-017-04650-4.
[52] T. Kondo, V. Mišík, and P. Riesz, "Sonochemistry of cytochrome c. Evidence for superoxide formation by ultrasound in argon-saturated aqueous solution," *Ultrason. Sonochem.*, vol. 3, no. 3, pp. S193–S199, Nov. 1996, doi: 10.1016/S1350-4177(96)00025-9.

2026 Sun Yat-sen University Science Award 仅用于2026年度中山大学科学奖公示

[53] J. Hahn, L. Krasnoperov, K. Luther, and J. Troe, “Pressure dependence of the reaction H + O2 (+Ar) → HO2 (+Ar) in the range 1–900 bar and 300–700 K,” *Phys. Chem. Chem. Phys.*, vol. 6, no. 9, pp. 1997–1999, Jan. 2004, doi: 10.1039/b404146a.
[54] Y. Han *et al.*, “A Perspective on Ultrasound-Triggered Production of Reactive Oxygen Species by Inorganic Nano/Microparticles,” *Adv. NanoBiomed Res.*, vol. 4, no. 9, p. 2400060, 2024, doi: 10.1002/anbr.202400060.
[55] B. H. J. Bielski, D. E. Cabelli, R. L. Arudi, and A. B. Ross, “Reactivity of HO2/O−2 Radicals in Aqueous Solution,” *J. Phys. Chem. Ref. Data*, vol. 14, no. 4, pp. 1041–1100, Oct. 1985, doi: 10.1063/1.555739.
[56] K. Yasui, “The Reducing Agents in Sonochemical Reactions without Any Additives,” *Molecules*, vol. 28, no. 10, p. 4198, May 2023, doi: 10.3390/molecules28104198.
[57] L. Zhang, M. Zhang, G. Kang, and Z. Xu, “Ultrasonically activated peroxymonosulfate oxidation for advanced water treatment: Cavitation mechanism, free radical generation and process simulation,” *Ultrason. Sonochem.*, vol. 122, p. 107601, Nov. 2025, doi: 10.1016/j.ultsonch.2025.107601.
[58] C. Kong *et al.*, “Ultrasound Irradiation-Induced Superoxide Anion Radical Mediates the Reduction of Tetravalent Platinum Prodrug for Antitumor Therapy,” *CCS Chem.*, vol. 7, no. 4, pp. 1142–1156, Jun. 2024, doi: 10.31635/ccschem.024.202404412.
[59] K. Murotomi, A. Umeno, M. Shichiri, M. Tanito, and Y. Yoshida, “Significance of Singlet Oxygen Molecule in Pathologies,” *Int. J. Mol. Sci.*, vol. 24, no. 3, p. 2739, Feb. 2023, doi: 10.3390/ijms24032739.
[60] M. Walker, A. J. A. Harvey, A. Sen, and C. E. H. Dessent, “Performance of M06, M06-2X, and M06-HF Density Functionals for Conformationally Flexible Anionic Clusters: M06 Functionals Perform Better than B3LYP for a Model System with Dispersion and Ionic Hydrogen-Bonding Interactions,” *J. Phys. Chem. A*, vol. 117, no. 47, pp. 12590–12600, Oct. 2013, doi: 10.1021/jp408166m.
[61] S. J. Pitman, A. K. Evans, R. T. Ireland, F. Lempriere, and L. K. McKemmish, “Reply to Comment on ‘Benchmarking Basis Sets for Density Functional Theory Thermochemistry Calculations: Why Unpolarized Basis Sets and the Polarized 6-311G Family Should Be Avoided,’” *J. Phys. Chem. A*, vol. 128, no. 36, pp. 7733–7738, Aug. 2024, doi: 10.1021/acs.jpca.4c03017.
[62] J. Lee *et al.*, “CHARMM-GUI Membrane Builder for Complex Biological Membrane Simulations with Glycolipids and Lipoglycans,” *J. Chem. Theory Comput.*, vol. 15, no. 1, pp. 775–786, Jan. 2019, doi: 10.1021/acs.jctc.8b01066.
[63] E. L. Wu *et al.*, “CHARMM-GUI Membrane Builder Toward Realistic Biological Membrane Simulations,” *J. Comput. Chem.*, vol. 35, no. 27, pp. 1997–2004, Oct. 2014, doi: 10.1002/jcc.23702.
[64] K. Vanommeslaeghe *et al.*, “CHARMM General Force Field (CGenFF): A force field for drug-like molecules compatible with the CHARMM all-atom additive biological force fields,” *J. Comput. Chem.*, vol. 31, no. 4, pp. 671–690, Mar. 2010, doi: 10.1002/jcc.21367.
[65] S. Kumar, J. M. Rosenberg, D. Bouzida, R. H. Swendsen, and P. A. Kollman, “THE weighted histogram analysis method for free-energy calculations on biomolecules. I. The method,” *J. Comput. Chem.*, vol. 13, no. 8, pp. 1011–1021, 1992, doi: 10.1002/jcc.540130812.

2026 S. -T. High School Science Award
仅用于2026日新闻学术奖公示

Acknowledgments

本研究得到了多方面的支持与指导，特此致谢。

感谢 BASIS Bilingual School Shenzhen 的 Dr. Shahid Ullah 和 Ms. Wendi Li 老师在本项研究的各个阶段提供的专业指导。Dr. Ullah 老师在项目初期帮助我理清研究思路，指导我从众多交叉学科前沿中精准选择了这一既具有学术创新性又具有临床应用价值的课题方向。Ms. Li 老师则在理论框架构建阶段，帮助我系统梳理了聚集诱导发光（AIE）的应用领域，使研究的科学性与严谨性得到了显著提升。在论文写作过程中，两位老师不仅对实验设计、数据呈现等学术规范提出了建设性意见，还耐心指导我如何将复杂的科学问题用清晰、简洁的语言表达。两位老师的专业建议与鼓励为本研究的顺利进行奠定了坚实的基础。

衷心感谢中国科学院深圳先进技术研究院生物医药与技术研究所纳米医疗技术中心为本研究提供的实验平台与技术支持。特别感谢张鹏飞副研究员和深圳市宝安区人民医院陈嘉婷博士的耐心指导与专业帮助。张博士在项目启动阶段为我详细讲解了 TTP-Mem 分子的合成路线与表征方法，陈博士则在弓形虫培养、感染模型建立等生物学实验方面给予了具体的技术指导。感谢深圳市华元生物技术股份有限公司 lncRNA 技术研究联合实验室为本研究提供的实验条件与便利。

在实验室老师的系统培训下，我从最初的完全陌生者逐步成长为能够独立完成实验的研究者。起初，我只是根据实验步骤进行合成，按照详细的 Protocol 一步步进行细胞复苏、传代培养等基础操作。但随着实验的深入，我开始理解每个操作背后的科学原理——PBS 的作用是什么？为什么要 37 度？为什么氢谱有杂峰，又该如何处理？我学会了不仅仅请教老师，更重要的是自己查阅文献、分析可能的原因、设计改进方案，在一次次失败的实验中成长。这个过程让我深刻体会到，科研工作的核心不是机械地重复实验步骤，而是在每一次操作中思考“为什么”。

更重要的是，在老师的一次次指导下，我开始将实验结果与书本上的理论相结合——开始自己推理反应机理，开始更深入的了解实验背后的原理。在分子动力学和高斯的的模拟中，我学会了超算的使用，并将我已有的计算机知识进行运用与跨学科的转移。

这段经历带给我的不仅是 TTP-Mem 制备、膜靶向特性表征、超声激活动力学疗法等具体的实验技能，更是对科学研究最真实的认识与热爱。

感谢父母长期以来对我科研兴趣的理解、支持与鼓励。正是他们的信任与帮助，让我能够联系到中国科学院深圳先进技术研究院这份宝贵的科研资源，为本项研究的顺利实施提供了坚强的后盾。父母不仅在物质上支持我往返实验室，更在精神上鼓励我克服科研中遇到的各种挑战。

2026 Intel High School Science Award
仅用于2026年英特尔高中科学奖公示